frontiers | Frontiers in Physics

ORIGINAL RESEARCH
published: 19 July 2022
doi: 10.3389/fphy.2022.915619

Diverse Exotic Orders and Fermiology in Fe-Based Superconductors: A Unified Mechanism for B_{1g}/B_{2g} Nematicity in FeSe/(Cs,Rb)Fe_2As_2 and Smectic Order in $BaFe_2As_2$

Seiichiro Onari and Hiroshi Kontani*

Department of Physics, Nagoya University, Nagoya, Japan

OPEN ACCESS

Edited by:
Laura Fanfarillo, International School for Advanced Studies (SISSA), Italy

Reviewed by:
Avraham Klein, Ariel University, Israel
Samuel Lederer, University of California, Berkeley, United States

***Correspondence:**
Seiichiro Onari
onari@s.phys.nagoya-u.ac.jp

Specialty section:
This article was submitted to Condensed Matter Physics, a section of the journal Frontiers in Physics

Received: *08 April 2022*
Accepted: *14 June 2022*
Published: *19 July 2022*

Citation:
Onari S and Kontani H (2022) Diverse Exotic Orders and Fermiology in Fe-Based Superconductors: A Unified Mechanism for B_{1g}/B_{2g} Nematicity in FeSe/(Cs,Rb)Fe_2As_2 and Smectic Order in $BaFe_2As_2$. Front. Phys. 10:915619. doi: 10.3389/fphy.2022.915619

A rich variety of nematic/smectic orders in Fe-based superconductors is an important unsolved problem in strongly correlated electron systems. A unified understanding of these orders has been investigated for the last decade. In this study, we explain the B_{1g} symmetry nematic transition in $FeSe_{1-x}Te_x$, the B_{2g} symmetry nematicity in AFe_2As_2 (A = Cs, Rb), and the smectic state in $BaFe_2As_2$ based on the same framework. We investigate the quantum interference mechanism between spin fluctuations by developing the density wave equation. The observed rich variety of nematic/smectic orders is naturally understood in this mechanism. The nematic/smectic orders depend on the characteristic shape and topology of the Fermi surface (FS) of each compound. 1) In $FeSe_{1-x}Te_x$ (n_d = 6.0), each FS is very small and the d_{xy}-orbital hole pocket is below the Fermi level. In this case, the small spin fluctuations on three d_{xz}, d_{yz}, and d_{xy} orbitals cooperatively lead to the B_{1g} nematic ($\boldsymbol{q} = \boldsymbol{0}$) order without magnetization. The experimental Lifshitz transition below the nematic transition temperature (T_S) is naturally reproduced. 2) In $BaFe_2As_2$ (n_d = 6.0), the d_{xy}-orbital hole pocket emerges around the M point, and each FS is relatively large. The strong spin fluctuations due to the d_{xy}-orbital nesting give rise to the B_{1g} nematic ($\boldsymbol{q} = \boldsymbol{0}$) order and the smectic [$\boldsymbol{q} = (0, \pi)$] order, and the latter transition temperature ($T^* \sim 170$K) exceeds the former one ($T_S \sim 140$K). 3) In heavily hole-doped AFe_2As_2 (n_d = 5.5), the large d_{xy}-orbital hole pocket and the four tiny Dirac pockets appear due to the hole-doping. The B_{2g} nematic bond order emerges on the d_{xy}-orbital hole pocket because of the same interference mechanism. The present paramagnon interference mechanism provides a unified explanation of why the variety of nematic/smectic orders in Fe-based superconductors is so rich, based on the well-established fermiology of Fe-based superconductors.

Keywords: nematic order, smectic order, orbital order, bond order, quantum critical point, iron-based superconductors

1 INTRODUCTION

The emergence of an electron nematic ($\boldsymbol{q} = \boldsymbol{0}$) state is one of the most important unsolved problems in Fe-based superconductors [1]. In LaFeAsO and Ba122 compounds, the antiferro (AF) magnetic state appears at the Néel temperature T_N, which is lower than the nematic transition temperature T_S. Since the superconducting phase with a high transition temperature (T_c) appears near the nematic phase and the AF magnetic phase, it is expected that the nematic fluctuations and the spin fluctuations are related to the mechanism of the high-T_c superconductivity. However, the questions appear before discussing the superconductivity: 1) what is the order parameter of the nematic state? 2) What is the driving force of the nematic state? 3) Why do the diverse nematic states emerge in various compounds?

It is known that the nematic order cannot be derived from the mean-field theory since the spin-channel order always dominates over the nematic order unless unphysical parameters (such as negative Hund's coupling) are assumed. Previously, to explain the nematic state [2], the vestigial order (spin nematic) scenario [3–9] and the orbital order scenario [10–22] have been proposed.

To investigate the nematic state, the FeSe family is an ideal platform since the AF magnetic state is absent [23–26]. This family is also ideal from the aspect of superconductivity since the highest $T_c \gtrsim 65$K in Fe-based superconductors has been reported in electron-doped FeSe [27–31]. In FeSe, the orbital polarization between d_{xz} and d_{yz} orbitals in the nematic state has been observed by angle-resolved-photoemission spectroscopy (ARPES) [32–36]. To be more precise, the orbital polarization energy $E_{xz} - E_{yz}$ has $\boldsymbol{k}$ dependence and changes the sign between the Γ point and the X (Y) point. This sign reversal orbital polarization has been explained by the orbital order scenario [16, 17, 19, 20] based on the paramagnon interference mechanism and by the renormalization group (RG) theory [37, 38]. In both theories, the vertex correction (VC) of the Coulomb interaction, which corresponds to the higher-order many-body effect, plays an essential role. Since the AF magnetic correlation is weak in FeSe, it is difficult to explain the nematic state by the vestigial order (spin nematic) scenario. Based on the paramagnon interference mechanism, the B_{1g} nematic orders in LaFeAsO and FeSe [14–18] and the nematic orders in cuprate superconductors [39–41] and magic-angle twisted bilayer graphene [42] have been explained as the orbital/bond orders. CDW orders in the transition metal dichalcogenide [43] and kagome metal [44] have also been explained by the paramagnon interference mechanism.

The rich variety of nematicity in the FeSe family remains a significant open problem. In $FeSe_{1-x}S_x$, T_S disappears at $x \sim 0.17$, where the emergence of the nematic quantum critical point (QCP) has been suggested by experiments [45–48]. Recently, the whole x dependent phase diagram for $FeSe_{1-x}Te_x$ ($x \lesssim 0.6$) has been reported [49–51]. In the phase diagram shown in **Figure 1A**, T_S decreases with Te doping x, and T_S disappears at $x \sim 0.5$. T_c becomes maximum ~ 15K at $x \sim 0.6$, which indicates that the nematic fluctuations enlarge the superconducting pairing interaction near the nematic QCP. Thus, it is essential to clarify the mechanism of x dependence of T_S to understand the mechanism of superconductivity in the FeSe family.

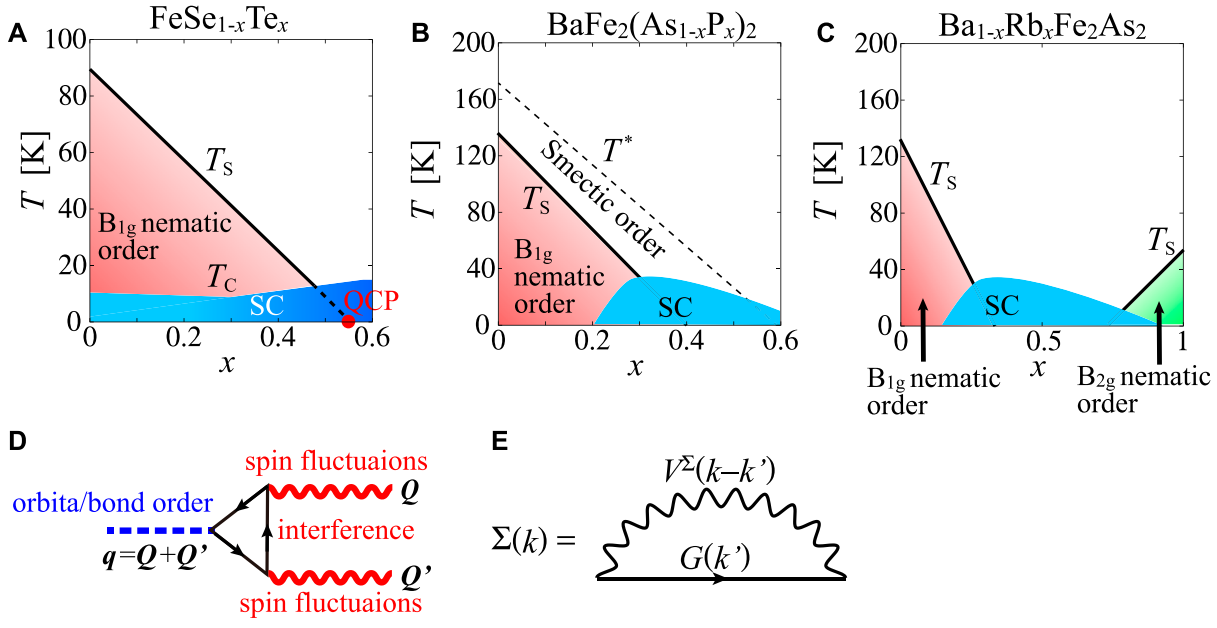

FIGURE 1 | (A) Schematic x-T phase diagram of $FeSe_{1-x}Te_x$, where T_S decreases with x, and T_c becomes maximum near the nematic QCP. **(B)** Schematic x-T phase diagram of $BaFe_2(As_{1-x}P_x)_2$, where tiny nematicity appears for $T_S < T < T^*$. We explain that "tiny nematicity" above T_S originates from the smectic bond order in later sections. **(C)** Schematic x-T phase diagram of $Ba_{1-x}Rb_xFe_2As_2$. The B_{2g} nematic order appears for the heavily hole-doped region $x > 0.5$. **(D)** Feynman diagram of the paramagnon interference mechanism for the orbital/bond order. **(E)** Feynman diagram of self-energy $\Sigma(k)$.

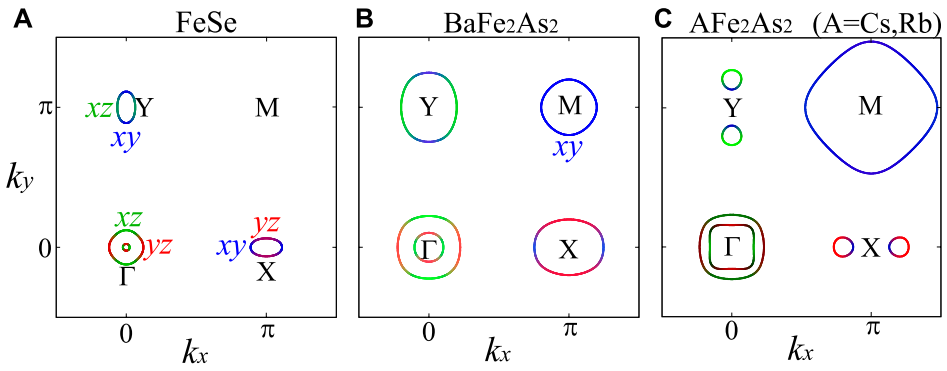

FIGURE 2 | FSs of **(A)** FeSe ($n_d = 6.0$), **(B)** $BaFe_2As_2$ ($n_d = 6.0$), and **(C)** AFe_2As_2 (A = Cs, Rb) ($n_d = 5.5$). The colors green, red, and blue correspond to orbitals 2, 3, and 4, respectively. A variety of nematic/smectic states originates from the characteristic structure of FSs.

In addition, a significant open issue in nematicity is the emergence of another type of nematicity in various Ba122 compounds below $T = T^*$, which is higher than T_S by tens of Kelvin, as shown in **Figure 1B**. An actual bulk nematic transition at $T = T^*$ has been reported in many experimental studies, such as a magnetic torque study [52], an X-ray study [53], an optical measurement study [54], and a laser photoemission electron microscope (PEEM) study [55]. Since the orthorhombicity $(a - b)/(a + b) \ll 0.1\%$ below T^* is tiny, an extrinsic origin such as inhomogeneity of the nematic transition temperature T_S due to local uniaxial pressure and randomness was proposed [4, 56–60]. On the other hand, T^* seems not to be sensitive to the sample quality and the local strain, and the domain structure of nematicity observed above T_S is homogeneous [54, 55]. It is noteworthy that bulk orbital polarization starts to emerge at $T = T^*(>T_S)$ in Ba122 compounds, according to the recent PEEM study [55]. In this study, we will explain the multistage smectic/nematic transitions: the smectic order ($\boldsymbol{q} \neq \boldsymbol{0}$) at $T = T^*$ and the nematic order ($\boldsymbol{q} = \boldsymbol{0}$) at T_S. In this scenario, T^* is given by the intrinsic smectic order free from randomness.

In contrast to B_{1g} nematicity in typical Fe-based superconductors, the emergence of 45°-rotated B_{2g} nematicity in heavily hole-doped AFe_2As_2 (A = Cs, Rb) has been reported in Refs. [61–64], while Refs. [65, 66] have reported the absence of the nematic order. As shown in **Figure 1C**, the dominant B_{1g} nematicity changes to B_{2g} nematicity with doping x in $Ba_{1-x}Rb_xFe_2As_2$. As for the mechanism of B_{2g} nematicity, vestigial nematic order by using the double-stripe magnetic configuration was suggested [67]. However, no SDW transition has been observed [64, 68] in AFe_2As_2, and the spin fluctuations are weak around T_S in $RbFe_2As_2$ [69]. In this study, we reveal the emergence of B_{2g}-symmetry bond order in AFe_2As_2.

As described previously, the variety of nematicity in Fe-based superconductors is very rich. To understand the mechanism of nematic/smectic states and superconductivity, it is important to explain these nematic/smectic states in the same theoretical framework.

In this study, we study B_{1g} nematicity in $FeSe_{1-x}Te_x$ ($n_d = 6.0$), the tiny nematicity below T^* in $BaFe_2As_2$ ($n_d = 6.0$), and B_{2g} nematicity in AFe_2As_2 (A = Cs, Rb) ($n_d = 5.5$) by developing the density wave (DW) equation theory. In this theory, the paramagnon interference mechanism due to the Aslamazov–Larkin (AL) type VCs shown in **Figure 1D** is taken into account. We also take into account of the self-energy effect shown in **Figure 1E**. In this mechanism, the rich variety of nematicity is naturally understood. The obtained nematicity depends on the shape and topology of FSs, as shown in **Figures 2A–C**. 1) In $FeSe_{1-x}Te_x$, all FSs are very small, and d_{xy}-orbital hole pocket is absent. The small spin fluctuations on the three d_{xz}, d_{yz}, and d_{xy} orbitals cooperatively lead to the B_{1g} nematic order, where the orbital order for d_{xz} and d_{yz} orbitals coexists with the bond order for the d_{xy} orbital. The experimental Lifshitz transition below T_S is naturally explained by the nematic order. 2) In $BaFe_2As_2$, the d_{xy} hole pocket emerges, and each FS is relatively large. The smectic order at $T = T^*(>T_S)$ and the nematic order at $T = T_S$ emerge due to the strong d_{xy}-orbital nesting. The smectic order explains the tiny nematicity below T^*, and the multistage transitions are explained by the smectic and nematic orders. 3) In heavily hole-doped AFe_2As_2, the large d_{xy}-orbital hole pocket and the four tiny Dirac pockets appear. The B_{2g} nematic bond order emerges due to the d_{xy}-orbital paramagnon interference mechanism, where the nesting between the Dirac pockets and the large d_{xy}-orbital hole pocket plays an important role. By considering the fermiology of each compound, these various nematic/smectic states are explained by the same theoretical framework based on the paramagnon interference mechanism.

In the present study, we intensively study the effect of self-energy on the nematic/smectic orders. It has been dropped in many previous studies, despite the fact that self-energy is necessary to satisfy the criteria of Baym–Kadanoff's conserving approximation [70, 71]. We revealed that 1) the nematic/smectic order is stabilized by the AL-type VCs, while 2) T_S is reduced to become realistic (~ 100K) by introducing self-energy. These results validate the idea of the "nematic/smectic state due to the paramagnon interference mechanism" proposed in our

previous studies [14–20, 39–44]. In addition, 3) the phase diagram of $FeSe_{1-x}Te_x$ [49–51] is understood by using a fixed Coulomb interaction because of self-energy (in the absence of self-energy, add-hoc doping x dependence of the Coulomb interaction has to be introduced). The main merits (1)–(3) in the present study strongly indicate that the nematic/smectic states originate from the paramagnon interference mechanism [14–20, 39–44].

2 MULTIORBITAL MODELS AND FORMULATION

2.1 Multiorbital Models

Here, we introduce multiorbital models based on the first principle's calculations. We analyze the following two-dimensional d-p Hubbard model with a unique parameter r, which controls the strength of the Coulomb interaction [16]:

$$H_x = H_x^0 + rH^U, \tag{1}$$

where H_x^0 is the first-principle's model, and H^U is the Coulomb interaction for d-orbitals. We neglect the Coulomb interaction for p-orbitals. We denote the five Fe d-orbitals $d_{3z^2-r^2}$, d_{xz}, d_{yz}, and d_{xy}, $d_{x^2-y^2}$ as $l = 1, 2, 3, 4$, and 5, and three Se(As) p-orbitals p_x, p_y, and p_z as $l = 6$, 7, and 8. To obtain the model, we first use the WIEN2k [72] and Wannier90 [73] codes. Next, to reproduce the experimentally observed FSs, we introduce the $\boldsymbol{k}$-dependent shifts for orbital l, δE_l, by modifying the intra-orbital hopping parameters, as explained in Ref. [17]. In the $FeSe_{1-x}Te_x$ model, we shift the d_{xy}-orbital band and the $d_{xz/yz}$-orbital band at [Γ, M, X] points by [0eV, − 0.27 eV, + 0.40 eV] and [− 0.24 eV, 0 eV, + 0.13 eV], respectively. In the $BaFe_2As_2$ model, the shifts are absent. In the $CsFe_2As_2$ model, we shift the d_{xy}-orbital band and the $d_{xz/yz}$-orbital band at [Γ, M, X] points by [0 eV, + 0.40 eV, 0 eV] and [− 0.40 eV, 0 eV, + 0.10 eV], respectively.

We use the d-orbital Coulomb interaction introduced by the constraint random phase approximation (RPA) method in Ref. [74]. The Coulomb interactions for the spin and charge channels are generally given as

$$U^{\mathrm{s}}_{l_1,l_2;l_3,l_4} = \begin{cases} U_{l_1,l_1}, & l_1 = l_2 = l_3 = l_4 \\ U'_{l_1,l_2}, & l_1 = l_3 \neq l_2 = l_4 \\ J_{l_1,l_3}, & l_1 = l_2 \neq l_3 = l_4 \\ J_{l_1,l_2}, & l_1 = l_4 \neq l_2 = l_3 \\ 0, & \text{otherwise.} \end{cases} \tag{2}$$

$$U^{\mathrm{c}}_{l_1,l_2;l_3,l_4} = \begin{cases} -U_{l_1,l_1}, & l_1 = l_2 = l_3 = l_4 \\ U'_{l_1,l_2} - 2J_{l_1,l_2}, & l_1 = l_3 \neq l_2 = l_4 \\ -2U'_{l_1,l_3} + J_{l_1,l_3}, & l_1 = l_2 \neq l_3 = l_4 \\ -J_{l_1,l_2}, & l_1 = l_4 \neq l_2 = l_3 \\ 0. & \text{otherwise.} \end{cases} \tag{3}$$

The Hamiltonian of the Coulomb interaction is given as

$$H^U = -\sum_{\boldsymbol{k}\boldsymbol{k}'\boldsymbol{q},\sigma\sigma'} \sum_{l_1 l_2 l_3 l_4} \left(\frac{U^c + U^s \sigma\sigma'}{4}\right)_{l_1,l_2;l_3,l_4} \times c^{l_1\dagger}_{\boldsymbol{k}+\boldsymbol{q},\sigma} c^{l_2}_{\boldsymbol{k},\sigma} c^{l_3\dagger}_{\boldsymbol{k}'-\boldsymbol{q},\sigma'} c^{l_4}_{\boldsymbol{k}',\sigma'}, \tag{4}$$

where σ, $\sigma' = \pm 1$ denote spin.

By using the multiorbital Coulomb interaction, the spin (charge) susceptibility $\hat{\chi}^{s(c)}(q)$ for $q = (\boldsymbol{q}, \omega_m = 2m\pi T)$ is given by

$$\hat{\chi}^{s(c)}(q) = \hat{\chi}^0(q)\left[1 - \hat{U}^{s(c)}\hat{\chi}^0(q)\right]^{-1}, \tag{5}$$

where irreducible susceptibility is

$$\chi^0_{l,l';m,m'}(q) = -\frac{T}{N}\sum_k G_{l,m}(k+q) G_{m',l'}(k). \tag{6}$$

$\hat{G}(k)$ is the multiorbital Green function with the self-energy $\hat{\Sigma}$ and given as $\hat{G}(k) = [(i\epsilon_n + \mu)\hat{1} - \hat{h}^0(\boldsymbol{k}) - \hat{\Sigma}(k)]^{-1}$ for $= [\boldsymbol{k}, \epsilon_n = (2n+1)\pi T]$. Here, $\hat{h}^0(\boldsymbol{k})$ is the matrix expression of H^0, and μ is the chemical potential. The spin (charge) Stoner factor $\alpha_{s(c)}$ is defined as the maximum eigenvalue of $\hat{U}^{s(c)}\hat{\chi}^0(\boldsymbol{q}, 0)$. Since $\hat{\chi}^{s(c)}(q) \propto (1 - \alpha_{s(c)})^{-1}$ holds, spin (charge) fluctuations develop with increasing $\alpha_{s(c)}$, and $\alpha_{s(c)} = 1$ corresponds to the spin- (charge)-channel ordered state.

2.2 FLEX Approximation

Here, we introduce the multiorbital fluctuation exchange (FLEX) approximation [15, 75]. The FLEX approximation satisfies the conserving approximation formalism of Baym and Kadanoff [70, 71]. In the FLEX approximation, self-energy is given as

$$\hat{\Sigma}(k) = \frac{T}{N}\sum_{k'} \hat{V}^{\Sigma}(k-k')\hat{G}(k'), \tag{7}$$

which is shown by the Feynman diagram in **Figure 1E**. The effective interaction $\hat{V}^{\Sigma}$ for self-energy in the FLEX approximation is given as

$$\hat{V}^{\Sigma}(q) = \frac{3}{2}\hat{U}^s\hat{\chi}^s(q)\hat{U}^s + \frac{1}{2}\hat{U}^c\hat{\chi}^c(q)\hat{U}^c + \frac{3}{2}\hat{U}^s + \frac{1}{2}\hat{U}^c - \hat{U}^{\uparrow\downarrow}\hat{\chi}^0(q)\hat{U}^{\uparrow\downarrow} - \frac{1}{2}\hat{U}^{\uparrow\uparrow}\hat{\chi}^0(q)\hat{U}^{\uparrow\uparrow}, \tag{8}$$

where $\hat{U}^{\uparrow\downarrow} \equiv \frac{\hat{U}^c - \hat{U}^s}{2}$ and $\hat{U}^{\uparrow\uparrow} \equiv \frac{\hat{U}^c + \hat{U}^s}{2}$ are denoted. We set $\mu = 0$. $\hat{\chi}^{s(c)}(q)$, $\hat{\Sigma}(k)$, and $\hat{G}(k)$ are calculated self-consistently. In multiband systems, the FSs are modified from the original FSs because of the self-energy correction. To escape from this difficulty, we subtract the Hermite term $[\hat{\Sigma}(\boldsymbol{k}, +i0) + \hat{\Sigma}(\boldsymbol{k}, -i0)]/2$ from the original self-energy, which corresponds to the elimination of double-counting terms between the LDA and FLEX.

2.3 Density-Wave Equation

We derive the strongest charge-channel density-wave (DW) instability without assuming the order parameter and wave vector. For this purpose, we use the DW equation method developed in Refs. [16, 19, 76]. We obtain the optimized non-local form factor $\hat{f}^{\boldsymbol{q}}(k)$ with the momentum and orbital dependences by solving the following linearized DW equation shown in **Figure 3A**:

$$\lambda_{\boldsymbol{q}} f^{\boldsymbol{q}}_{l,l'}(k) = \frac{T}{N}\sum_{k',m,m'} K^{\boldsymbol{q}}_{l,l';m,m'}(k,k') f^{\boldsymbol{q}}_{m,m'}(k'), \tag{9}$$

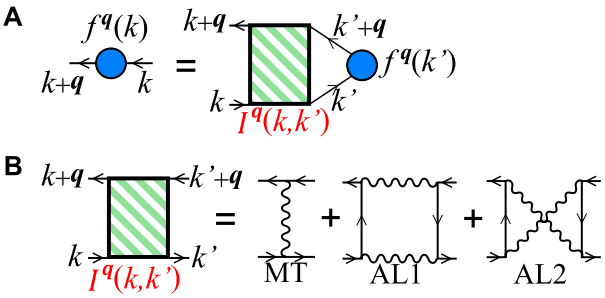

FIGURE 3 | Feynman diagrams of **(A)** DW equation and **(B)** charge-channel irreducible four-point vertex. Each wavy line represents a spin-fluctuation-mediated interaction.

$$K^{\boldsymbol{q}}_{l,l';m,m'}(k,k') = \sum_{m_1,m_2} I^{\boldsymbol{q}}_{l,l';m_1,m_2}(k,k') g^{\boldsymbol{q}}_{m_1,m_2;m,m'}(k'), \tag{10}$$

where $\lambda_{\boldsymbol{q}}$ is the eigenvalue of the form factor $\hat{f}^{\boldsymbol{q}}(k)$, $g^{\boldsymbol{q}}_{l,l';m,m'}(k) \equiv -G_{l,m}(k+\boldsymbol{q})G_{m',l'}(k)$, and $\hat{I}^{\boldsymbol{q}}(k,k')$ is the charge-channel irreducible four-point vertex shown in **Figure 3B**. The four-point vertex interaction $\hat{I}^{\boldsymbol{q}}(k,k')$ in the DW **Eq. 10** [16, 19] is given by

$$I^{\boldsymbol{q}}_{l,l';m,m'}(k,k') = \sum_{b=s,c}\Bigg[-\frac{a^b}{2}V^b_{l,m;l',m'}(k-k') + \frac{T}{N}\sum_{p,l_1,l_2,m_1,m_2}\frac{a^b}{2}V^b_{l,l_1;m,m_2}$$

$$(p+\boldsymbol{q})V^b_{m',l_2;l',m_1}(p)G_{l_1,m_1}(k-p)G_{l_2,m_2}(k'-p) \quad + \frac{T}{N}\sum_{p,l_1,l_2,m_1,m_2}\frac{a^b}{2}V^b_{l,l_1;l_2,m'}$$

$$(p+\boldsymbol{q})V^b_{m_2,m;l',m_1}(p)G_{l_1,m_1}(k-p)G_{l_2,m_2}(k'+p+\boldsymbol{q})\Bigg], \tag{11}$$

where $a^s = 3$, $a^c = 1$, $p = (\boldsymbol{p}, \omega_l)$, and $\hat{V}^{s(c)}(q) = \hat{U}^{s(c)} + \hat{U}^{s(c)}\hat{\chi}^{s(c)}(q)\hat{U}^{s(c)}$.

In **Eq. 11**, the first line corresponds to the Maki-Thompson (MT) term, and the second and third lines give the AL terms, respectively. Feynman diagrams of the MT terms and AL terms are shown in **Figure 3B**.

The AL terms are enhanced by the paramagnon interference $\chi^s(\boldsymbol{Q}) \times \chi^s(\boldsymbol{Q}')$ shown in **Figure 1D**. Thus, $\boldsymbol{q} = \boldsymbol{Q} + \boldsymbol{Q}' = \boldsymbol{0}$ nematic order is naturally induced by the paramagnon interference at the same nesting vector ($\boldsymbol{Q}' = -\boldsymbol{Q}$). In the MT term, the first-order term with respect to $\hat{U}^{s,c}$ gives the Hartree–Fock (HF) term in the mean-field theory. The charge-channel DW with wave vector $\boldsymbol{q}$ is established when the largest $\lambda_{\boldsymbol{q}} = 1$. Thus, the smaller $\lambda_{\boldsymbol{q}}$ corresponds to the lower T_S. DW susceptibility is proportional to $1/(1-\lambda_{\boldsymbol{q}})$ as explained in Ref. [20]. Therefore, $\lambda_{\boldsymbol{q}}$ represents the strength of the DW instability.

3 RESULTS AND DISCUSSIONS

3.1 Results of $FeSe_{1-x}Te_x$

In this section, we show that 1) the B_{1g} nematic orbital + bond order originates from the paramagnon interference, and 2) the effect of self-energy is essential to reproduce the x dependence of T_S as shown in **Figure 1A** in $FeSe_{1-x}Te_x$. The effect of self-energy on the nematic/smectic order caused by the VCs is systematically studied in the present work. Because of self-energy, T_S is reduced to become realistic (~ 100K), while the symmetry of the nematic/smectic order is unchanged. Thus, the idea of electronic nematicity due to "the paramagnon-interference mechanism" proposed in Refs. [14–20, 39–44] has been confirmed by the present study.

Hereafter, we fix $r = 0.35$, $T = 15$ meV in calculations with self-energy and $r = 0.15$, $T = 15$ meV in calculations without the self-energy, unless otherwise noted.

Figures 4A,B show x dependent FSs and band structures, respectively. The FSs are small compared to other Fe-based superconductors. The d_{xy} orbital level E^M_{xy} at the M point increases with increasing x, as shown in **Figure 4C**. This behavior is consistent with ARPES measurements [77, 78]. On the other hand, the d_{xy} orbital level E^Γ_{xy} at the Γ point decreases with increasing x. E^Γ_{xy} becomes lower than the $d_{xz(yz)}$ orbital level for $x \gtrsim 0.3$, and the topology of band changes. The change in topology has been observed between Γ and Z points in ARPES measurements of $FeSe_{0.5}Te_{0.5}$ [79, 80]. **Figure 4D** shows the density of state (DOS) of orbitals 3 and 4 for $x = 0$, 0.5. The DOS near the Fermi level for $x = 0.5$ is larger than that for $x = 0$ since the bandwidth decreases, and E^M_{xy} comes close to the Fermi level with increasing x. In addition, the dispersion of orbitals 2 and 3 at the Γ point becomes flat as E^Γ_{xy} decreases with increasing x, which also enlarges the DOS for orbitals 2 and 3 near the Fermi level.

To discuss the self-energy effect, we calculate the mass enhancement factors. **Figure 5** shows the obtained x dependence of the mass enhancement factors $z_l^{-1}(\pi,0)$ for orbital $l = 3$, 4, which are given by $z_l^{-1}(\boldsymbol{k}) = 1 - \mathrm{Im}\Sigma_{l,l}(\boldsymbol{k},\pi T)/\pi T$ in the FLEX approximation. The value of $z_l^{-1}(\pi,0)$ increases with increasing x since the electron correlation increases due to the reduction in the bandwidth and the increase in the DOS as shown in **Figure 4D**. Particularly, $z_4^{-1}(\pi,0)$ is enhanced by the d_{xy} orbital electron correlation between the electron pockets and the band around the M point since E^{M}_{xy} comes close to the Fermi level, as shown in **Figure 4C**. The behaviors of z_l^{-1} are similar to those given by the dynamical mean-field theory [81] and experiment [82].

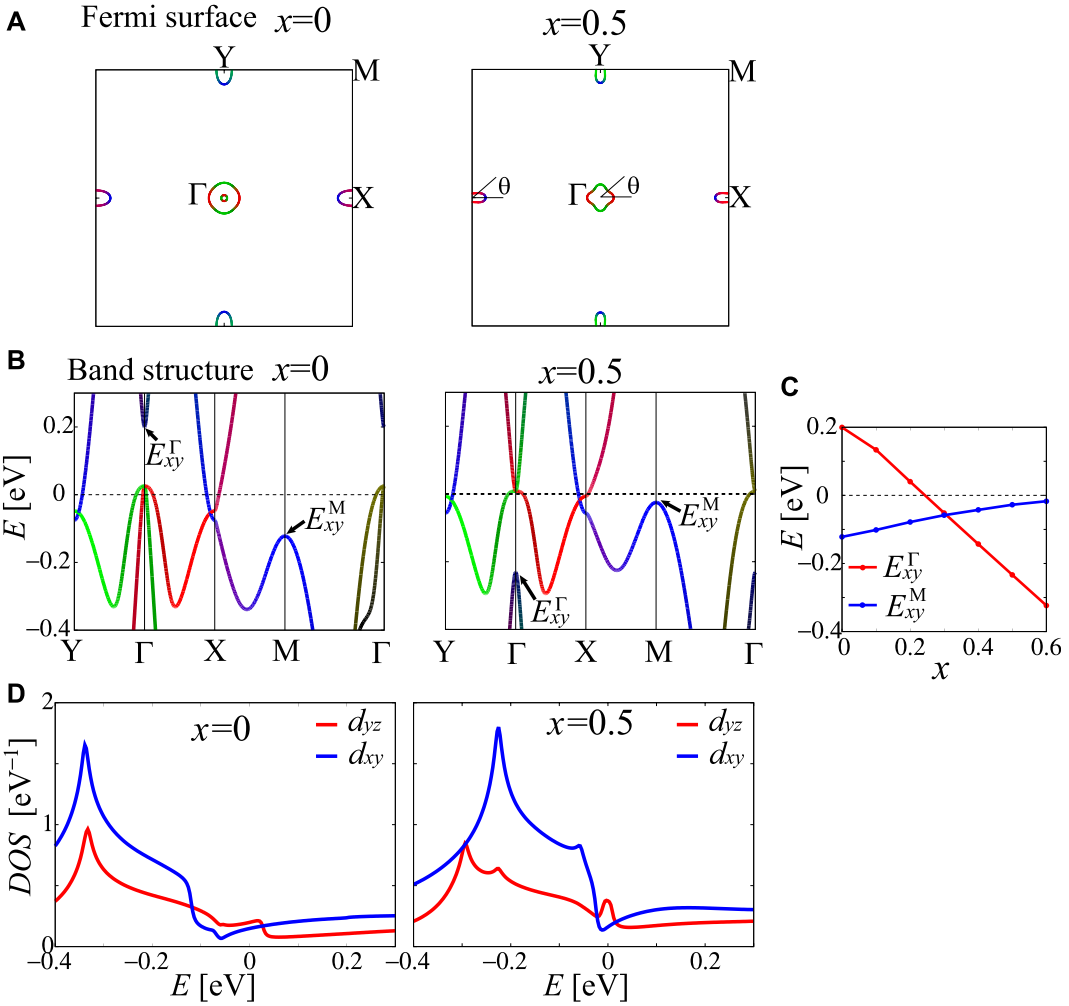

FIGURE 4 | (A) FSs and **(B)** band structures of $FeSe_{1-x}Te_x$ for $x = 0$ and 0.5. **(C)** x dependences of E^{Γ}_{xy} and E^{M}_{xy}. **(D)** DOS of orbitals 3 and 4 for $x = 0, 0.5$.

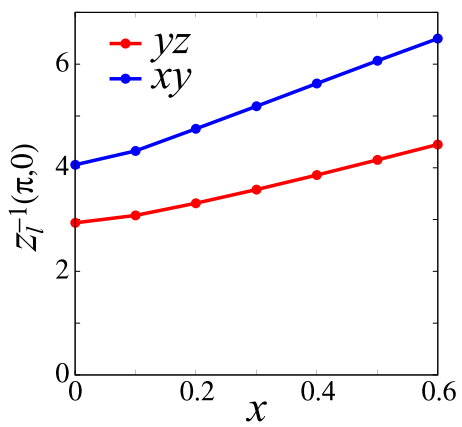

FIGURE 5 | x dependences of the mass enhancement factor $z_l^{-1}(\pi, 0)$ for orbitals $l = 3$ and 4.

Figure 6 shows x dependences of $\chi^s_{3,3;3,3}(\pi, 0)$ and $\chi^s_{4,4;4,4}(\pi, 0)$ in the FLEX approximation and the RPA. $\chi^s_{3,3;3,3}(\pi, 0)$ is almost independent of doping x, which means that change in topology or the number of FS around Γ comprising d_{xz} and d_{yz} orbitals does not strongly affect the spin fluctuation for the $d_{xz(yz)}$ orbital. On the other hand, $\chi^s_{4,4;4,4}(\pi, 0)$ in the RPA without self-energy is strongly enhanced with increasing x since the electron correlation for the d_{xy} orbital between electron pockets and the band around the M point is significant for the enhancement of $\chi^s_{4,4;4,4}(\pi, 0)$. The strong enhancement of $\chi^s_{4,4;4,4}(\pi, 0)$ is suppressed by the self-energy in the FLEX approximation. This suppression is necessary to reproduce the x dependence of T_S in the phase diagram.

Hereafter, we discuss the DW instability given by the DW **Eq. 9**. **Figure 7A** shows x dependences of λ_0 for the B_{1g} nematic state with and without the self-energy. λ_0 without the self-energy rapidly increases with doping x due to the paramagnon interference shown in **Figure 1D**. λ_0 is enlarged by the

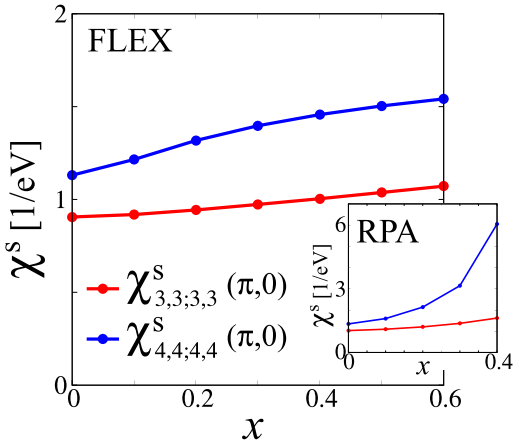

FIGURE 6 | x dependences of $\chi^s_{3,3;3,3(4,4;4,4)}(\pi,0)$ in the FLEX approximation. Those in the RPA are shown in the inset.

interference between $\chi^s_{4,4;4,4}$ strongly enhanced in the RPA, as shown in **Figure 6**. Since this result means T_S increases with x, the phase diagram in **Figure 1A** cannot be explained when the self-energy is absent. However, λ_0 including the self-energy decreases with doping x since the enhancement of $\chi^s_{4,4;4,4}$ in the FLEX approximation is moderate and the self-energy suppresses the $\hat{G}$ and $\hat{I}$ in the DW **Eq. 10**. The value of λ_0 increases with decreasing T, as shown in **Figure 7B**, and $T = T_S$ is given when $\lambda_0 = 1$ is satisfied. Thus, T_S at $x = 0$ is higher than that at $x = 0.5$, and T_S at $x = 0.65$ cannot be obtained for $T > 6$ meV. The x dependence of T_S obtained by the paramagnon interference mechanism is consistent with the phase diagram in **Figure 1A** [49]. We see that T dependences of the strength of nematic fluctuations $1/(1 - \lambda_0)$ satisfy the Curie–Weiss law at low temperatures, as shown in **Figure 7C**. We note that the B_{1g} nematic state is realized because of the small FSs even for the weak spin fluctuations [16, 17].

Here, we analytically explain that T_S is reduced by self-energy by focusing on the mass renormalization factor z. As discussed in Ref. [17], $\alpha_{s(c)}$ is independent of z under the scaling $T \to zT$ and $r \to r/z$. Under this scaling, the eigenvalue of the DW equation is unchanged [17]. Thus, T_S obtained by the DW equation without the self-energy is reduced to zT_S because of the self-energy. As a result, realistic T_S is obtained by taking self-energy into account.

Figure 8A shows $\boldsymbol{q}$ dependences of $\lambda_{\boldsymbol{q}}$ with the self-energy at $x = 0, 0.5$. $\lambda_{\boldsymbol{q}}$ has peak at $\boldsymbol{q} = \boldsymbol{0}$, which means that the ferro nematic order is favored. **Figure 8B** shows $\boldsymbol{k}$ dependences of the static form factors $f^{\boldsymbol{0}}_{33}(\boldsymbol{k})$ and $f^{\boldsymbol{0}}_{44}(\boldsymbol{k})$, where $\hat{f}^{\boldsymbol{q}}(\boldsymbol{k})$ is given by the analytic continuation of $\hat{f}^{\boldsymbol{q}}(k)$. $f^{\boldsymbol{0}}_{33}(k_x, k_y) = -f^{\boldsymbol{0}}_{22}(k_y, k_x)$ represents B_{1g} orbital order between orbitals 2 and 3. From the $\boldsymbol{k}$ dependence of $f^{\boldsymbol{0}}_{33(22)}(\boldsymbol{k})$, the sign-reversing orbital order is confirmed along the $k_x(k_y)$ axis. As shown in **Figure 8C**, $\boldsymbol{k}$ dependence of $f^{\boldsymbol{0}}_{44}(\boldsymbol{k}) \propto \cos(k_x) - \cos(k_y)$ causes the B_{1g} nearest-neighbor bond order, which is the modulation of correlated hopping. Based on the paramagnon interference mechanism, we find that the small spin fluctuations on the three d_{xz}, d_{yz}, and d_{xy} orbitals cooperatively cause the B_{1g} nematic orbital + bond order. The FSs and the band structure under the nematic order with the maximum value of the form factor $f^{\boldsymbol{0}}_{\max} = 80$meV are shown in **Figures 8D,E**. $f^{\boldsymbol{0}}_{\max} = 80$meV with the mass enhancement factor $z_l^{-1} = 2 \sim 4$ is consistent with ARPES measurements [35, 36]. The Lifshitz transition, where the FS around the Y point is missing, has been reported in recent experiments [83–86]. The Lifshitz transition is naturally explained by the increase of the d_{xy} level around the Y point induced by $f^{\boldsymbol{0}}_{44}(\boldsymbol{k})$. We note that the obtained coexistence of the bond order on the d_{xy} orbital and the orbital order on the (d_{xz}, d_{yz}) orbitals has already been shown in the supplementary material of Refs. [19, 20]. In **Figure 8D**, we derived the Lifshitz transition by setting $f^{\boldsymbol{0}}_{\max} = 80$meV by hand. It is noteworthy that the same result is recently obtained by solving the full DW equation in Ref. [87]. The full DW equation enables us to study the electronic states below T_S without introducing additional fitting parameters.

Here, we confirm that the d_{xy} orbital levels at Γ and M points are important for the x dependence of λ_0. We use the simple model, where only the shift of E^{Γ}_{xy} or E^{M}_{xy} is introduced for the $x = 0$ model. **Figure 9A** shows E^{Γ}_{xy} dependences of $z_l^{-1}(\pi, 0)$ and λ_0,

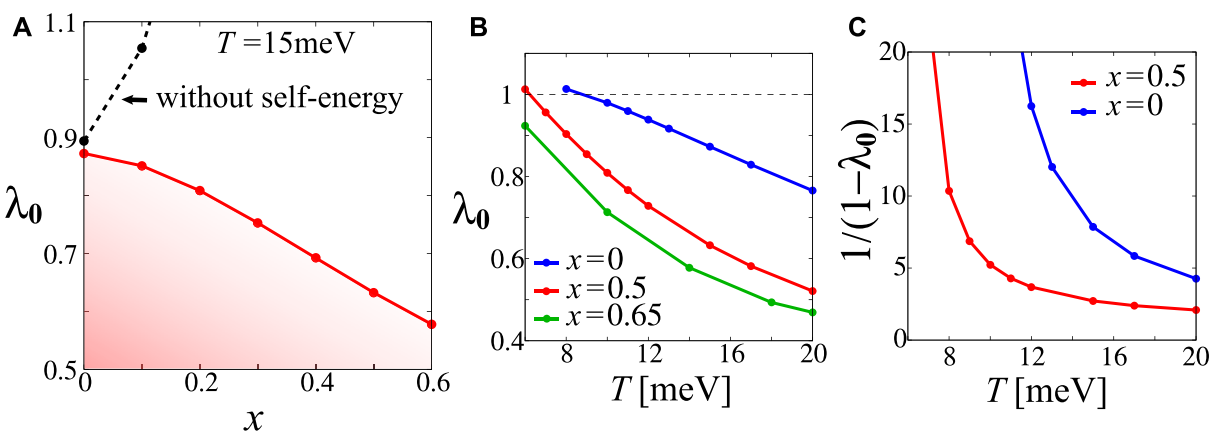

FIGURE 7 | (A) x dependences of λ_0 in the DW equation with and without self-energy at $T = 15$ meV. **(B)** T dependences of λ_0 with self-energy for $x = 0, 0.5, 0.65$. **(C)** T dependences of $1/(1 - \lambda_0)$ with self-energy for $x = 0, 0.5$.

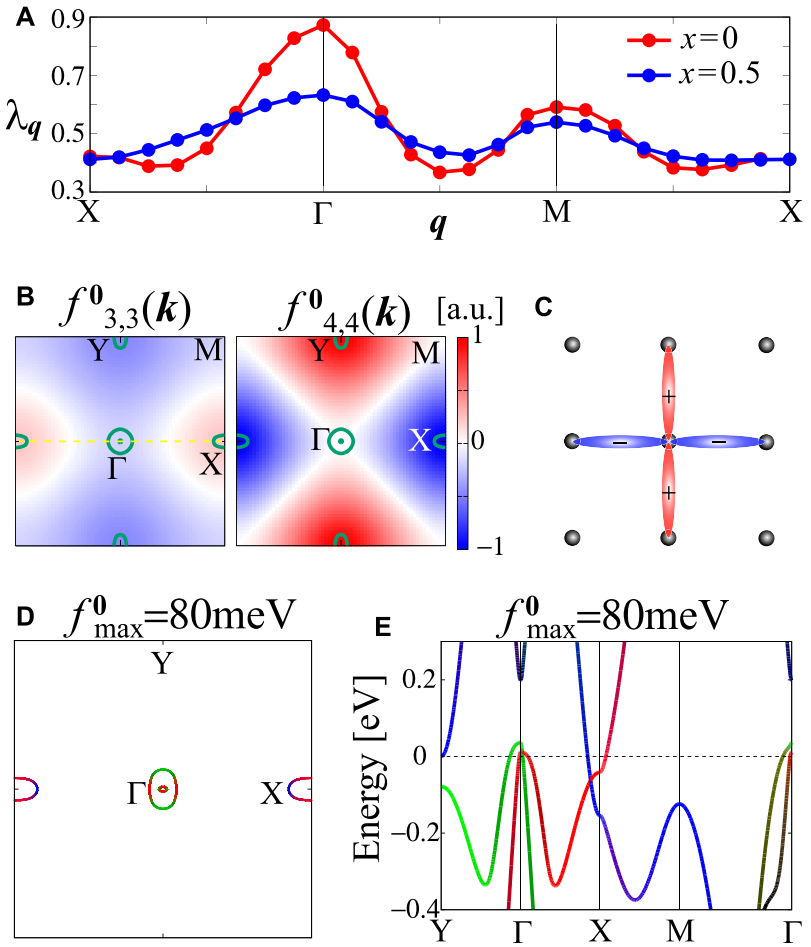

FIGURE 8 | (A) q dependences of λ_q with self-energy for $x = 0$, 0.5. **(B)** k dependences of $f^0_{3,3}(k)$ and $f^0_{4,4}(k)$ for $x = 0$, where green lines denote FSs. $f^0_{3,3}(k)$ changes sign along the k_x axis (yellow dashed line). **(C)** B_{1g} nearest-neighbor bond order corresponding to $f^0_{4,4}(k)$. **(D)** FSs and **(E)** band structure under the nematic order with f^0_{max} = 80meV for $x = 0$.

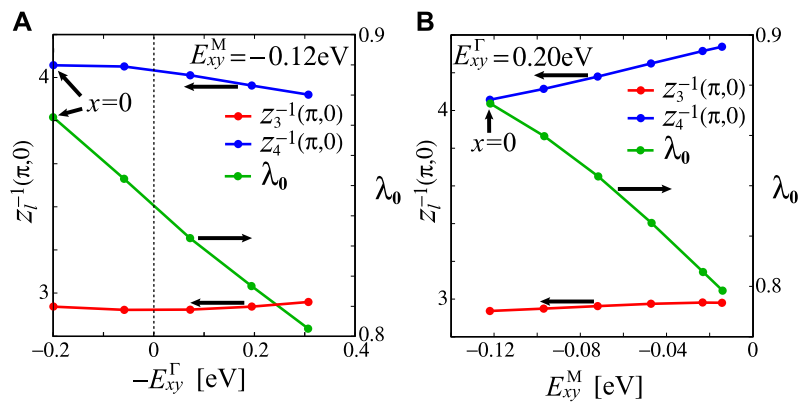

FIGURE 9 | (A) E^Γ_{xy} dependences of $z_l^{-1}(\pi,0)$ for $l = 3$, 4, and λ_0 given by introducing only E^Γ_{xy} shift for the $x = 0$ model. **(B)** E^M_{xy} dependences of $z_l^{-1}(\pi,0)$ for $l = 3$, 4, and λ_0 given by introducing only E^M_{xy} shift for the $x = 0$ model.

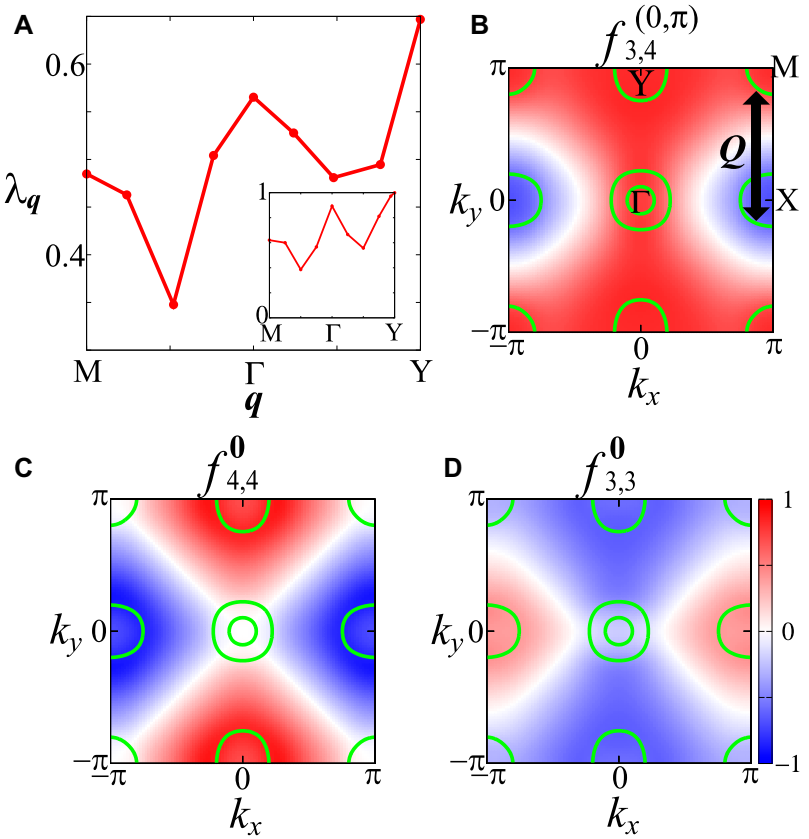

FIGURE 10 | (A) $\boldsymbol{q}$ dependence of $\lambda_{\boldsymbol{q}}$ with self-energy for $r = 0.68$ at $T = 5$ meV in $BaFe_2As_2$, and that without self-energy for $r = 0.30$ at $T = 32.4$ meV in the inset. **(B)** $\boldsymbol{k}$ dependence of the dominant form factor at $\boldsymbol{q} = (0, \pi)$, $f^{\boldsymbol{q}}_{3,4}(\boldsymbol{k})$ with self-energy, which is given by the off-diagonal orbitals 3 and 4. $\boldsymbol{k}$ dependences of form factors at $\boldsymbol{q} = \boldsymbol{0}$, **(C)** $f^{\mathbf{0}}_{4,4}(\boldsymbol{k})$, and **(D)** $f^{\mathbf{0}}_{3,3}(\boldsymbol{k})$ with self-energy. Green lines denote FSs.

respectively. $z_l^{-1}(\pi, 0)$ is almost independent of the value of E^{Γ}_{xy}. $\lambda_{\mathbf{0}}$ decreases with decreasing E^{Γ}_{xy}, which is consistent with the result shown in **Figure 7A**. The topology of the band structure changes at the Γ point with decreasing E^{Γ}_{xy}, which plays an important role in decreasing $\lambda_{\mathbf{0}}$. **Figure 9B** shows E^{M}_{xy} dependences of $z_l^{-1}(\pi, 0)$ and $\lambda_{\mathbf{0}}$, respectively. The behaviors of $z_4^{-1}(\pi, 0)$ and $\lambda_{\mathbf{0}}$ are similar to the results shown in **Figure 5**, **Figure 7A**. The x dependences of $z_4^{-1}(\pi, 0)$ and $\lambda_{\mathbf{0}}$ are explained by the electron correlation between the electron pockets and the d_{xy} band around the M point. $\lambda_{\mathbf{0}}$ is suppressed by self-energy for the d_{xy} orbital. The suppression becomes strong with increasing E^{M}_{xy} due to the feedback effect of the self-energy. To summarize, the B_{1g} nematic orbital + bond order is explained by the paramagnon interference mechanism in $FeSe_{1-x}Te_x$, and x dependence of T_S is well reproduced by the self-energy effect for the d_{xy} orbital.

3.2 Results of $BaFe_2As_2$

In this section, we discuss the multi-nematicity in $BaFe_2As_2$ [20].

The effect of self-energy on the nematic/smectic orders caused by the VCs is studied in the present work. Transition temperatures are reduced to become realistic because of the self-energy, while the symmetries of the nematic/smectic orders are unchanged. We reveal the origin of the tiny nematicity below $T = T^*$ and explain the multistage transitions at $T = T^*$ and T_S in the phase diagram shown in **Figure 1B**. As shown in **Figure 2B**, the size of the hole FS around the M point comprising the d_{xy} orbital is similar to that of electron FSs around the X and Y points, which causes good intra- and inter-orbital nestings. As explained later, inter-orbital nesting is important to realize the smectic state at $T = T^*$.

Figure 10A shows the $\boldsymbol{q}$-dependence of $\lambda_{\boldsymbol{q}}$ with and without self-energy. The $\boldsymbol{q} = (0, \pi)$ smectic bond order is dominant over the $\boldsymbol{q} = \boldsymbol{0}$ nematic orbital + bond order because of the relation $\lambda_{(0,\pi)} > \lambda_{\mathbf{0}}$, which is robust in the presence of moderate spin fluctuations $\alpha_s \gtrsim 0.85$. Thus, the nematic orbital + bond transition temperature T_S is lower than T^*, where the smectic bond order appears. **Figure 10B** shows the dominant component of the static form factor, $f^{\boldsymbol{q}}_{3,4}(\boldsymbol{k})$, for $\boldsymbol{q} = (0, \pi)$. Focusing on the X and M points, $f^{(0,\pi)}_{3,4}(\boldsymbol{k})$ is proportional to $-\cos(k_y)$, which corresponds to the inter-orbital smectic bond order, where the y-direction hoppings between orbitals 3 and 4 are modulated by the correlated hopping $\delta t_{3,4}(y;\, y \pm 1) = -\delta t_{4,3}(y;\, y \pm 1) = \delta t(-1)^y$. It is to be noted that $\delta t_{l,m}(y;\, y')$ is real and equal to $\delta t_{m,l}(y';\, y)$.

As shown in **Figure 1D**, the origin of the smectic bond order $f^{(0,\pi)}_{3,4}$ is the quantum interference between the spin fluctuations $\chi^s(\boldsymbol{Q})$ for $\boldsymbol{Q} \approx (0, \pi)$ and $\chi^s(\boldsymbol{0})$ due to the AL terms. In this case, $\boldsymbol{q} = (0, \pi)$ $(= \boldsymbol{Q} + \boldsymbol{Q}')$ is given by $\boldsymbol{Q}' = \boldsymbol{0}$. $\chi^s(\boldsymbol{Q})$ is enhanced when the FS appears around the M point since nesting between FSs around the

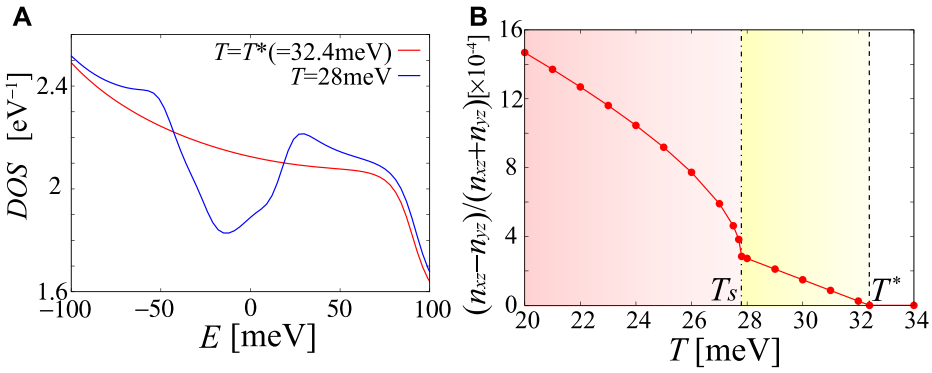

FIGURE 11 | (A) DOS at $T = T^* = 32.4$ meV and that at $T = 28$ meV($<T^*$), including the smectic bond order. **(B)** T dependence of nematicity $\psi = (n_2 - n_3)/(n_2 + n_3)$ including both the smectic-bond order for $T < T^*$ and the ferro-orbital/bond order for $T < T_S$.

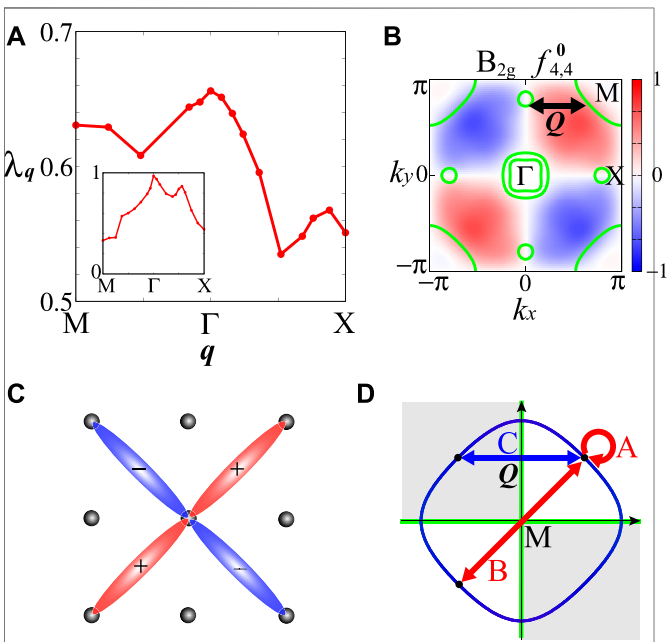

FIGURE 12 | (A) $\boldsymbol{q}$ dependence of $\lambda_{\boldsymbol{q}}$ with self-energy in $CsFe_2As_2$, and that without self-energy in the inset. **(B)** $\boldsymbol{k}$ dependence of the B_{2g} form factor $f^{\boldsymbol{0}}_{4,4}(\boldsymbol{k}) \propto \sin(k_x)\sin(k_y)$, where the green lines and black arrow denote FSs and nesting vector $\boldsymbol{Q} \sim (0.5\pi, 0)$, respectively. **(C)** B_{2g} next-nearest-neighbor bond order corresponding to the $f^{\boldsymbol{0}}_{4,4}(\boldsymbol{k})$. **(D)** B_{2g} form factor $\propto \sin(k_x)\sin(k_y)$ driven by the attractive interactions (red arrows) A and B, and the repulsive interaction (blue arrow) C in the DW equation, where green lines denote nodes in the B_{2g} form factor.

X and M points becomes good, while the moderate $\chi^s(\boldsymbol{0})$ is caused by forward scattering. We find that $f^{(0,\pi)}_{3,4}$ is significantly enlarged by inter-orbital nesting between the d_{xy}-orbital FS around the M point and the d_{yz}-orbital FS around the X point. In addition to the quantum interference due to the AL terms, the MT terms strengthen the sign change of $f^{(0,\pi)}_{3,4}(\boldsymbol{k})$ between the X and M points, as reported previously [16, 19, 37]. Thus, the smectic bond order originates from the cooperation between the AL and MT terms due to good inter-orbital nesting between FSs around the X and M points. In contrast, the B_{1g} nematic orbital + bond order shown in **Figures 10C,D** originates from the interference between $\chi^s(\boldsymbol{Q})$ and $\chi^s(-\boldsymbol{Q})$. This nematic orbital + bond order is similar to that in FeSe and $FeSe_{1-x}Te_x$.

Here, we examine the DOS under the smectic bond order to verify the present theory. For $T < T^* = 32.4$ meV without self-energy, we introduce the mean-field-like T-dependent form factor $\hat{f}^{\boldsymbol{q}}(T) = f^{\max}\tanh(1.74\sqrt{T^*/T-1})\hat{f}^{\boldsymbol{q}}$, where $\hat{f}^{\boldsymbol{q}}$ is the obtained form factor for $\boldsymbol{q} = (0, \pi)$ normalized as $\max_{\boldsymbol{k}}|f^{\boldsymbol{q}}(\boldsymbol{k})| = 1$. We put $f^{\max} = 60$ meV. **Figure 11A** shows the DOS at $T = T^*$ and 28 meV($<T^*$). For $T < T^*$, a pseudogap appears due to the smectic bond order, which is consistent with the experiments [88, 89]. Since the smectic bond order is an antiferroic order, the folded band structure emerges below T^*, which is also consistent with the experiment [90].

Next, we focus on another mystery, the T-linear behavior of tiny nematicity ψ in Ba122 [52] below T^*. To solve this mystery, we calculate the T dependence of uniform nematicity $\psi = (n_2 - n_3)/(n_2 + n_3)$ in **Figure 11B**, where both $\hat{f}^{(0,\pi)}(T)$ for $T < T^*$ and the ferro nematic orbital + bond order $\hat{f}^{\boldsymbol{0}}(T)$ for $T < T_S = 27.8$meV) are introduced. For $T < T_S$, we assume $\hat{f}^{\boldsymbol{0}}(T) = f^{\max}\tanh(1.74\sqrt{T_S/T-1})\hat{f}^{\boldsymbol{0}}$, where $\hat{f}^{\boldsymbol{0}}$ is the obtained form factor normalized as $\max_{\boldsymbol{k}}|f^{\boldsymbol{0}}(\boldsymbol{k})| = 1$. We use $f^{\max} = 60$ meV, which corresponds to the $d_{xz(yz)}$ orbital energy split ~ 60meV in the ARPES measurements [91] by considering the mass enhancement factor $z_l^{-1} \sim 2$ for $l = 2, 3$. The T-linear behavior $\psi \propto (T^* - T)$ for $T_S < T < T^*$ is a consequence of the relation $\psi \propto [f^{(0,\pi)}(T)]^2$ because the $f^{(0,\pi)}$ term cannot contribute to any $\boldsymbol{q} = \boldsymbol{0}$ linear response. It is to be noted that the form factor $\hat{f}^{(\pi,0)}$ for $\boldsymbol{q} = (\pi, 0)$ gives $\psi < 0$. Thus, the T-linear behavior of ψ below T^* is also naturally explained by the smectic bond order. On the other hand, $\psi \propto \sqrt{T_S - T}$ for $T < T_S$ is induced by the nematic orbital + bond order. To summarize, the multistage transitions at $T = T^*$ and T_S, and the T-linear ψ below T^*, are naturally explained by the smectic bond order and nematic orbital + bond order. The hole pocket around the M point is necessary to realize the smectic bond order by the paramagnon interference mechanism.

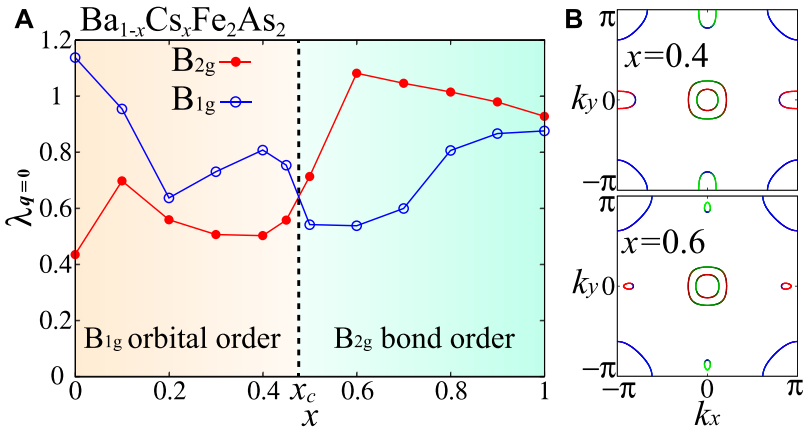

FIGURE 13 | (A) x dependences of $\lambda_{q=0}$ without self-energy for B_{1g} and B_{2g} symmetries in $Ba_{1-x}Cs_xFe_2As_2$. **(B)** FSs for $x = 0.4$ and $x = 0.6$. The dominant nematic order changes at $x = x_c \sim 0.5$ near the Lifshitz transition, where the electron FSs split into the four tiny Dirac pockets.

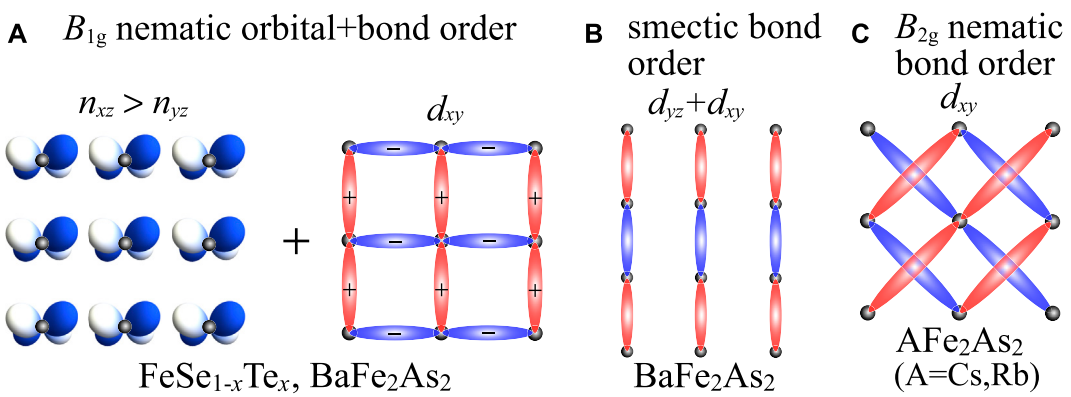

FIGURE 14 | (A) Schematic picture of the B_{1g} nematic orbital + bond order in $FeSe_{1-x}Te_x$ and $BaFe_2As_2$, where the orbital order for the d_{xz} and d_{yz} orbitals coexists with the bond order for the d_{xy} orbital. **(B)** Schematic picture of the smectic bond order for d_{yz} and d_{xy} orbitals in $BaFe_2As_2$. **(C)** Schematic picture of the B_{2g} nematic bond order for the d_{xy} orbital in AFe_2As_2 (A = Cs, Rb).

We stress that the present mechanism of the bulk nematicity for $T_S < T < T^*$ is intrinsic and free from the strength of the disorder and local strain in the system. The present smectic order originates from the AL–VC and the FS nesting between the d_{xy}-orbital hole pocket and the electron pockets [20]. We stress that the present theory explains the absence of the smectic order in bulk FeSe [55] because the d_{xy}-orbital hole pocket, which is necessary for smectic order formation, is below the Fermi level in FeSe.

Here, we explain the details of the recent microscopic measurements in P-doped Ba122 [54, 55] that support the present intrinsic scenario. These are bulk and real-space measurements. In the PEEM measurement [55], very uniform bulk nematic domains have been observed for $T_S < T < T^*$. The width of each nematic domain is about 500 nm. The structure of the nematic domains is unchanged for $T < T_S$. In addition, once the nematic domain completely disappears by increasing T, it never appears at the same location if the temperature is lowered again. These results are consistent with the present intrinsic smectic order scenario for $T_S < T < T^*$ in P-doped Ba122. In the photo-modulation measurement [54], uniform nematic domains have also been observed. The observed nematicity becomes small near the nematic domain boundary, irrespective of the fact that large local strain anisotropy is observed at the domain boundary. The observed anticorrelation between the nematicity and the local strain anisotropy may conflict with the assumption of the extrinsic scenario of the nematicity above T_S.

In contrast, the extrinsic scenario has been proposed by other groups [4, 56–60]. In the extrinsic mechanism, nematicity for $T > T_S$ in Co-doped Ba122, which exhibits large residual resistivity (>100 $\mu\Omega cm$), has been explained by the inhomogeneity of T_S induced by the disorder and local strain. However, it is not easy to explain the nematicity above T_S in clean P-doped (non-doped) Ba122 on the same footing in the extrinsic scenario.

We note that the multistage smectic/nematic transitions observed in NaFeAs [92] are also explained by the present intrinsic mechanism [20].

3.3 Results of $Ba_{1-x}Cs_xFe_2As_2$

In this section, we discuss B_{2g} nematicity in heavily hole-doped compound AFe_2As_2 (A = Cs, Rb) [19]. The effect of self-energy on the nematic order caused by the VCs is studied in the present work. Because of self-energy, T_S is reduced to become realistic, whereas the symmetry of the nematic order is unchanged. The direction of B_{2g} nematicity is rotated by 45° from that of the conventional B_{1g} nematicity. **Figure 2C** shows FSs of $CsFe_2As_2$: the hole FS around the M point comprising the d_{xy}-orbital is large, whereas the Dirac pockets near the X and Y points are small. In this system, the d_{xy}-orbital spin fluctuations are dominant.

Figure 12A shows the $\boldsymbol{q}$ dependence of the largest eigenvalue $\lambda_{\boldsymbol{q}}$ with self-energy for $r = 0.96$ at $T = 5$ meV and that without self-energy for $r = 0.30$ at $T = 20$ meV $\lambda_{\boldsymbol{q}}$ becomes maximum at $\boldsymbol{q} = \boldsymbol{0}$ and the dominant form factor $f^{\boldsymbol{0}}_{4,4}(\boldsymbol{k}) \propto \sin(k_x)\sin(k_y)$ at $\boldsymbol{q} = \boldsymbol{0}$ is shown in **Figure 12B**. As shown in **Figure 12C**, this form factor corresponds to the B_{2g} next-nearest-neighbor bond order for the d_{xy} orbital, which is consistent with the experimentally observed B_{2g} nematicity [61–64]. By analyzing the irreducible four-point vertex $I^{\boldsymbol{0}}_{4,4;4,4}(k,k')$ in the DW **Eq. 10**, we find that the attractive (repulsive) interactions originate from the AL (MT) terms, as shown in **Figure 12D**. The obtained $\boldsymbol{q} = \boldsymbol{0}$ B_{2g} bond order is derived from these interactions. Since the AL terms are enhanced by the quantum interference between the spin fluctuations with $\boldsymbol{Q}$ and $\boldsymbol{Q}'(= -\boldsymbol{Q})$, as shown in **Figure 1D**, the $\boldsymbol{q} = \boldsymbol{0}$ nematic bond order is realized. The value of $\lambda_{\boldsymbol{0}}$ is strongly enhanced by the attractive interactions for the d_{xy} orbital due to the AL terms. In this system, the nesting vector is short $\boldsymbol{Q} \sim (0.5\pi, 0)$, as shown in **Figure 12B**. Because of repulsive interaction by the MT terms, $f^{\boldsymbol{0}}_{4,4}(\boldsymbol{k})$ changes sign between the $\boldsymbol{k}$ points on the FSs connected by $\boldsymbol{Q}$, as shown in **Figure 12D**. To summarize, the AL terms strongly enlarge $\lambda_{\boldsymbol{0}}$ due to the paramagnon interference mechanism, and the MT terms favor B_{2g} symmetry. Cooperation of the AL and MT terms is important to realize the B_{2g} bond order.

We comment on the recent experiments on $RbFe_2As_2$. The specific heat jump at $T_S = 40$K ($\Delta C/T_S$) is very small [64]. However, it is naturally understood based on the recent theoretical scaling relation $\Delta C/T_S \propto T_S^b$ with $b \sim 3$ derived in Ref. [87]. Although the smallness of B_{2g} nematic susceptibility in $RbFe_2As_2$ was recently reported in Refs. [65, 66], the field angle-dependent specific heat measurement has shown finite B_{2g} nematicity above T_c [93]. Further experimental and theoretical studies are necessary to clarify the nematicity in AFe_2As_2 (A = Cs, Rb).

Finally, we discuss the x dependence of nematicity in $Ba_{1-x}A_xFe_2As_2$ (A = Cs, Rb). The schematic phase diagram of $Ba_{1-x}Rb_xFe_2As_2$ given by the experiment [64] is shown in **Figure 1C**. We introduce the model Hamiltonian for $Ba_{1-x}Cs_xFe_2As_2$, by interpolating between the $BaFe_2As_2$ model and the $CsFe_2As_2$ model with the ratio $1 - x$: x. **Figure 13A** shows x dependences of $\lambda_{\boldsymbol{q}=\boldsymbol{0}}$ without self-energy for the B_{2g} and the B_{1g} symmetries by fixing $T = 30$ meV and $r = 0.30$. Below $x = x_c \sim 0.5$, the B_{1g} nematic orbital order is dominant as discussed in the previous section, while the B_{2g} nematic bond order dominates over the B_{1g} nematic orbital order for $x > x_c$. As shown in **Figure 13B**, the Lifshitz transition occurs at $x \sim x_c$, where the electron pockets split into the four tiny Dirac pockets. Thus, the B_{2g} nematic bond order appears when the nesting vector $\boldsymbol{Q}$ between the electron pockets and hole pocket around the M point becomes short $\boldsymbol{Q} \sim (0.5\pi, 0)$. By taking account of the Lifshitz transition at $x \sim x_c$, the schematic phase diagram in **Figure 1C** is also well reproduced by the orbital/bond order because of the paramagnon interference mechanism. We note that the $\boldsymbol{q} = (0, \pi)$ smectic order is dominant over the $\boldsymbol{q} = \boldsymbol{0}$ B_{1g} nematic order at $x = 0$, as shown in the previous section.

4 CONCLUSION

We discussed the rich variety of nematic/smectic states in Fe-based superconductors in the same theoretical framework based on the paramagnon interference mechanism. In this mechanism, the charge-channel order is induced by the quantum interference between the spin fluctuations, as shown in **Figure 1D**. The form factor and wave vector of the DW instability are derived from the DW equation based on the paramagnon interference mechanism. Recently, a rigorous formalism of the DW equation has been constructed based on the Luttinger–Ward (LW) theory in Ref. [87]. According to Ref. [87], the solution of the DW equation gives the minimum of the grand potential in the LW theory. Thus, the nematic/smectic order discussed in the present study is thermodynamically stable in the framework of the conserving approximation.

By considering the characteristic fermiology of each compound, the paramagnon interference mechanism explains the rich variety of the nematic/smectic states. In **Figures 14A–C**, we summarized the nematic/smectic orders revealed by the mechanism in the present study. 1) In $FeSe_{1-x}Te_x$, each FS is very small and the d_{xy}-orbital hole pocket is absent. In this case, the small spin fluctuations on the three orbitals cooperatively lead to the B_{1g} orbital order for the d_{xz} and d_{yz} orbitals coexisting with the d_{xy}-orbital bond order, as shown in **Figure 14A**. The nematic orbital + bond order causes the Lifshitz transition, where the FS around the Y point disappears, which is consistent with the recent experiments. The x dependence of T_S in the phase diagram is reproduced by introducing self-energy. 2) In $BaFe_2As_2$, the d_{xy}-orbital hole pocket emerges. Since each electron and hole pocket is relatively large and similar in size, the strong d_{xy}-orbital spin fluctuations due to good nesting give rise to the smectic order shown in **Figure 14B** and the B_{1g} nematic order. The smectic order explains the tiny T-linear nematicity below $T = T^*(> T_S)$. We predict the multistage transitions with the smectic order at $T = T^*$ and the nematic order at T_S. 3) In heavily hole-doped AFe_2As_2 (A = Cs, Rb), the tiny Dirac pockets around the X(Y) point and the large d_{xy}-orbital hole pocket appear due to hole-doping. The B_{2g} bond order for the d_{xy} orbital shown in **Figure 14C** emerges due to the d_{xy}-orbital paramagnon interference mechanism. The B_{2g} bond order is triggered by the Lifshitz transition of the electron FSs by hole-doping.

The limitation of this theory is that the calculated VCs are reduced to an infinite series of the MT and AL terms. To verify the validity of the present theory, we performed the functional renormalization group (fRG) analysis for the single-orbital Hubbard model for

cuprates [41] and the two-orbital Hubbard model for ruthenates [94], and obtained the bond-order (orbital order) in the former (latter) model. These results are consistent with previous experiments, and they are also obtained by the DW equation analysis. In the fRG theory, a huge number of higher-order VCs are generated in an unbiased manner by solving the RG equation. Thus, the significance of the MT and AL terms in the present theory has been confirmed by the different and excellent theoretical frameworks.

In future, it is to clarify the mechanism of superconductivity and non-Fermi-liquid behaviors of transport phenomena in the FeSe family by considering the nematic fluctuations enlarged near the nematic QCP. This issue will be discussed in future studies [95].

DATA AVAILABILITY STATEMENT

The original contributions presented in the study are included in the article; further inquiries can be directed to the corresponding author.

AUTHOR CONTRIBUTIONS

SO performed all calculations with contributions from HK. SO and HK wrote the manuscript.

FUNDING

This work was supported by Grants-in-Aid for Scientific Research from MEXT, Japan (No.s JP19H05825, JP18H01175, and JP17K05543), and Nagoya University Research Fund.

ACKNOWLEDGMENTS

We acknowledge Y. Yamakawa, R. Tazai, and S. Matsubara for their collaboration in the theoretical studies. We are grateful to Y. Matsuda, T. Hanaguri, T. Shibauchi, S. Kasahara, T. Shimojima, and Y. Mizukami for useful discussions about experiments.

REFERENCES

1. Hosono H, Kuroki K. Iron-based Superconductors: Current Status of Materials and Pairing Mechanism. *Physica C: Superconductivity its Appl* (2015) 514: 399–422. doi:10.1016/j.physc.2015.02.020
2. Hirschfeld PJ, Korshunov MM, Mazin II. Gap Symmetry and Structure of Fe-Based Superconductors. *Rep Prog Phys* (2011) 74:124508. doi:10.1088/0034-4885/74/12/124508
3. Fernandes RM, VanBebber LH, Bhattacharya S, Chandra P, Keppens V, Mandrus D, et al. Effects of Nematic Fluctuations on the Elastic Properties of Iron Arsenide Superconductors. *Phys Rev Lett* (2010) 105:157003. doi:10.1103/PhysRevLett.105.157003
4. Fernandes RM, Abrahams E, Schmalian J. Anisotropic In-Plane Resistivity in the Nematic Phase of the Iron Pnictides. *Phys Rev Lett* (2011) 107:217002. doi:10.1103/PhysRevLett.107.217002
5. Wang F, Kivelson SA, Lee D-H. Nematicity and Quantum Paramagnetism in FeSe. *Nat Phys* (2015) 11:959–63. doi:10.1038/nphys3456
6. Yu R, Si Q. Antiferroquadrupolar and Ising-Nematic Orders of a Frustrated Bilinear-Biquadratic Heisenberg Model and Implications for the Magnetism of FeSe. *Phys Rev Lett* (2015) 115:116401. doi:10.1103/PhysRevLett.115.116401
7. Glasbrenner JK, Mazin II, Jeschke HO, Hirschfeld PJ, Fernandes RM, Valentí R. Effect of Magnetic Frustration on Nematicity and Superconductivity in Iron Chalcogenides. *Nat Phys* (2015) 11:953–8. doi:10.1038/nphys3434
8. Fang C, Yao H, Tsai WF, Hu J, Kivelson SA. Theory of Electron Nematic Order in LaFeAsO. *Phys Rev B* (2008) 77:224509. doi:10.1103/PhysRevB.77.224509
9. Fernandes RM, Chubukov AV. Low-energy Microscopic Models for Iron-Based Superconductors: a Review. *Rep Prog Phys* (2017) 80:014503. doi:10.1088/1361-6633/80/1/014503
10. Krüger F, Kumar S, Zaanen J, van den Brink J. Spin-orbital Frustrations and Anomalous Metallic State in Iron-Pnictide Superconductors. *Phys Rev B* (2009) 79:054504. doi:10.1103/PhysRevB.79.054504
11. Lv W, Wu J, Phillips P. Orbital Ordering Induces Structural Phase Transition and the Resistivity Anomaly in Iron Pnictides. *Phys Rev B* (2009) 80:224506. doi:10.1103/physrevb.80.224506
12. Lee CC, Yin WG, Ku W. Ferro-Orbital Order and Strong Magnetic Anisotropy in the Parent Compounds of Iron-Pnictide Superconductors. *Phys Rev Lett* (2009) 103:267001. doi:10.1103/PhysRevLett.103.267001
13. Kontani H, Onari S. Orbital-Fluctuation-Mediated Superconductivity in Iron Pnictides: Analysis of the Five-Orbital Hubbard-Holstein Model. *Phys Rev Lett* (2010) 104:157001. doi:10.1103/PhysRevLett.104.157001
14. Onari S, Kontani H. Self-consistent Vertex Correction Analysis for Iron-Based Superconductors: Mechanism of Coulomb Interaction-Driven Orbital Fluctuations. *Phys Rev Lett* (2012) 109:137001. doi:10.1103/PhysRevLett.109.137001
15. Onari S, Yamakawa Y, Kontani H. High-TcSuperconductivity Near the Anion Height Instability in Fe-Based Superconductors: Analysis ofLaFeAsO1−xHx. *Phys Rev Lett* (2014) 112:187001. doi:10.1103/PhysRevLett.112.187001
16. Onari S, Yamakawa Y, Kontani H. Sign-Reversing Orbital Polarization in the Nematic Phase of FeSe Due to theC2Symmetry Breaking in the Self-Energy. *Phys Rev Lett* (2016) 116:227001. doi:10.1103/physrevlett.116.227001
17. Yamakawa Y, Onari S, Kontani H. Nematicity and Magnetism in FeSe and Other Families of Fe-Based Superconductors. *Phys Rev X* (2016) 6:021032. doi:10.1103/PhysRevX.6.021032
18. Yamakawa Y, Kontani H. Nematicity, Magnetism, and Superconductivity in FeSe under Pressure: Unified Explanation Based on the Self-Consistent Vertex Correction Theory. *Phys Rev B* (2017) 96:144509. doi:10.1103/PhysRevB.96.144509
19. Onari S, Kontani H. Origin of Diverse Nematic Orders in Fe-Based Superconductors: 45° Rotated Nematicity in AFe_2As_2(A=Cs,Rb). *Phys Rev B* (2019) 100:020507(R). doi:10.1103/physrevb.100.020507
20. Onari S, Kontani H. Hidden Antiferronematic Order in Fe-Based Superconductor BaFe2As2 and NaFeAs above TS. *Phys Rev Res* (2020) 2: 042005(R). doi:10.1103/PhysRevResearch.2.042005
21. Jiang K, Hu J, Ding H, Wang Z. Interatomic Coulomb Interaction and Electron Nematic Bond Order in FeSe. *Phys Rev B* (2016) 93:115138. doi:10.1103/PhysRevB.93.115138
22. Fanfarillo L, Giovannetti G, Capone M, Bascones E. Nematicity at the Hund's Metal Crossover in Iron Superconductors. *Phys Rev B* (2017) 95:144511. doi:10.1103/PhysRevB.95.144511
23. Hsu FC, Luo JY, Yeh KW, Chen TK, Huang TW, Wu PM, et al. Superconductivity in the PbO-type Structure α-FeSe. *Proc Natl Acad Sci U.S.A* (2008) 105:14262–4. doi:10.1073/pnas.0807325105
24. Böhmer AE, Kreisel A. Nematicity, Magnetism and Superconductivity in FeSe. *J Phys Condens Matter* (2018) 30:023001. doi:10.1088/1361-648X/aa9caa
25. Kreisel A, Hirschfeld P, Andersen B. On the Remarkable Superconductivity of FeSe and its Close Cousins. *Symmetry* (2020) 12:1402. doi:10.3390/sym12091402
26. Shibauchi T, Hanaguri T, Matsuda Y. Exotic Superconducting States in FeSe-Based Materials. *J Phys Soc Jpn* (2020) 89:102002. doi:10.7566/jpsj.89.102002
27. Wang QY, Li Z, Zhang WH, Zhang ZC, Zhang JS, Li W, et al. Interface-Induced High-Temperature Superconductivity in Single Unit-Cell FeSe Films on SrTiO 3. *Chin Phys. Lett.* (2012) 29:037402. doi:10.1088/0256-307x/29/3/037402
28. Ge JF, Liu ZL, Liu C, Gao CL, Qian D, Xue QK, et al. Superconductivity above 100 K in Single-Layer FeSe Films on Doped SrTiO3. *Nat Mater* (2015) 14: 285–9. doi:10.1038/nmat4153

29. Fan Q, Zhang WH, Liu X, Yan YJ, Ren MQ, Peng R, et al. Plain S-Wave Superconductivity in Single-Layer FeSe on SrTiO3 Probed by Scanning Tunnelling Microscopy. *Nat Phys* (2015) 11:946–52. doi:10.1038/nphys3450
30. Zhang Y, Lee JJ, Moore RG, Li W, Yi M, Hashimoto M, et al. Superconducting gap Anisotropy in Monolayer FeSe Thin Film. *Phys Rev Lett* (2016) 117: 117001. doi:10.1103/PhysRevLett.117.117001
31. Miyata Y, Nakayama K, Sugawara K, Sato T, Takahashi T. High-temperature Superconductivity in Potassium-Coated Multilayer FeSe Thin Films. *Nat Mater* (2015) 14:775–9. doi:10.1038/nmat4302
32. Shimojima T, Suzuki Y, Sonobe T, Nakamura A, Sakano M, Omachi J, et al. Lifting of *Xz/yz* Orbital Degeneracy at the Structural Transition in Detwinned FeSe. *Phys Rev B* (2014) 90:121111(R). doi:10.1103/physrevb.90.121111
33. Nakayama K, Miyata Y, Phan GN, Sato T, Tanabe Y, Urata T, et al. Reconstruction of Band Structure Induced by Electronic Nematicity in an FeSe Superconductor. *Phys Rev Lett* (2014) 113:237001. doi:10.1103/physrevlett.113.237001
34. Suzuki Y, Shimojima T, Sonobe T, Nakamura A, Sakano M, Tsuji H, et al. Momentum-dependent Sign Inversion of Orbital Order in Superconducting FeSe. *Phys Rev B* (2015) 92:205117. doi:10.1103/PhysRevB.92.205117
35. Zhang Y, Yi M, Liu ZK, Li W, Lee JJ, Moore RG, et al. Distinctive Orbital Anisotropy Observed in the Nematic State of a FeSe Thin Film. *Phys Rev B* (2016) 94:115153. doi:10.1103/PhysRevB.94.115153
36. Yi M, Pfau H, Zhang Y, He Y, Wu H, Chen T, et al. Nematic Energy Scale and the Missing Electron Pocket in FeSe. *Phys Rev X* (2019) 9:041049. doi:10.1103/PhysRevX.9.041049
37. Xing RQ, Classen L, Chubukov AV. Orbital Order in FeSe: The Case for Vertex Renormalization. *Phys Rev B* (2018) 98:041108(R). doi:10.1103/PhysRevB.98.041108
38. Chubukov AV, Khodas M, Fernandes RM. Magnetism, Superconductivity, and Spontaneous Orbital Order in Iron-Based Superconductors: Which Comes First and Why? *Phys Rev X* (2016) 6:041045. doi:10.1103/PhysRevX.6.041045
39. Kawaguchi K, Yamakawa Y, Tsuchiizu M, Kontani H. Competing Unconventional Charge-Density-Wave States in Cuprate Superconductors: Spin-Fluctuation-Driven Mechanism. *J Phys Soc Jpn* (2017) 86:063707. doi:10.7566/jpsj.86.063707
40. Yamakawa Y, Kontani H. Spin-Fluctuation-Driven Nematic Charge-Density Wave in Cuprate Superconductors: Impact of Aslamazov-Larkin Vertex Corrections. *Phys Rev Lett* (2015) 114:257001. doi:10.1103/PhysRevLett.114.257001
41. Tsuchiizu M, Kawaguchi K, Yamakawa Y, Kontani H. Multistage Electronic Nematic Transitions in Cuprate Superconductors: A Functional-Renormalization-Group Analysis. *Phys Rev B* (2018) 97:165131. doi:10.1103/physrevb.97.165131
42. Onari S, Kontani H. SU(4) Valley+Spin Fluctuation Interference Mechanism for Nematic Order in Magic-Angle Twisted Bilayer Graphene: The Impact of Vertex Corrections. *Phys Rev Lett* (2022) 128:066401. doi:10.1103/PhysRevLett.128.066401
43. Hirata T, Yamakawa Y, Onari S, Kontani H. Unconventional Orbital Charge Density Wave Mechanism in the Transition Metal Dichalcogenide 1T−TaS2. *Phys Rev Res* (2021) 3:L032053. doi:10.1103/physrevresearch.3.l032053
44. Tazai R, Yamakawa Y, Onari S, Kontani H. Mechanism of Exotic Density-Wave and Beyond-Migdal Unconventional Superconductivity in Kagome Metal AV 3 Sb 5 (A = K, Rb, Cs). *Sci Adv* (2022) 8:eabl4108. doi:10.1126/sciadv.abl4108
45. Licciardello S, Buhot J, Lu J, Ayres J, Kasahara S, Matsuda Y, et al. Electrical Resistivity across a Nematic Quantum Critical point. *Nature* (2019) 567:213–7. doi:10.1038/s41586-019-0923-y
46. Coldea AI, Blake SF, Kasahara S, Haghighirad AA, Watson MD, Knafo W, et al. Evolution of the Low-Temperature Fermi Surface of Superconducting FeSe1−xSx across a Nematic Phase Transition. *Npj Quant Mater* (2019) 4:2. doi:10.1038/s41535-018-0141-0
47. Huang WK, Hosoi S, Čulo M, Kasahara S, Sato Y, Matsuura K, et al. Magnetization Switching Driven by Current-Induced Torque from Weakly Spin-Orbit Coupled Zr. *Phys Rev Res* (2020) 2:033367. doi:10.1103/PhysRevResearch.2.033367
48. Huang WK, Hosoi S, Čulo M, Kasahara S, Sato Y, Matsuura K, et al. Non-Fermi Liquid Transport in the Vicinity of the Nematic Quantum Critical point of Superconducting FeSe1−xSx. *Phys Rev Res* (2020) 2:033367. doi:10.1103/PhysRevResearch.2.033367
49. Mukasa K, Matsuura K, Qiu M, Saito M, Sugimura Y, Ishida K, et al. High-pressure Phase Diagrams of FeSe1−xTex: Correlation between Suppressed Nematicity and Enhanced Superconductivity. *Nat Commun* (2021) 12:381. doi:10.1038/s41467-020-20621-2
50. Mukasa K, Ishida K, Imajo S, Qiu MW, Saito M, Matsuura K, et al. Enhanced Superconducting Pairing Strength Near a Nonmagnetic Nematic Quantum Critical point. *ArXiv* (2022) 2202:11657. doi:10.48550/arXiv.2202.11657
51. Ishida K, Onishi Y, Tsujii M, Mukasa K, Qiu M, Saito M, et al. Pure Nematic Quantum Critical point Accompanied by a Superconducting Dome. *ArXiv* (2022) 2202:11674. doi:10.1073/pnas.2110501119
52. Kasahara S, Shi HJ, Hashimoto K, Tonegawa S, Mizukami Y, Shibauchi T, et al. Electronic Nematicity above the Structural and Superconducting Transition in BaFe2(As1−xP X)2. *Nature* (2012) 486:382–5. doi:10.1038/nature11178
53. Kim YK, Jung WS, Han GR, Choi KY, Chen CC, Devereaux TP, et al. Existence of Orbital Order and its Fluctuation in SuperconductingBa(Fe1−xCox) 2As2Single Crystals Revealed by X-ray Absorption Spectroscopy. *Phys Rev Lett* (2013) 111:217001. doi:10.1103/physrevlett.111.217001
54. Thewalt E, Hayes IM, Hinton JP, Little A, Patankar S, Wu L, et al. Imaging Anomalous Nematic Order and Strain in Optimally Doped $BaFe_2(As,P)_2$. *Phys Rev Lett* (2018) 121:027001. doi:10.1103/physrevlett.121.027001
55. Shimojima T, Motoyui Y, Taniuchi T, Bareille C, Onari S, Kontani H, et al. Discovery of Mesoscopic Nematicity Wave in Iron-Based Superconductors. *Science* (2021) 373:1122–5. doi:10.1126/science.abd6701
56. Chu JH, Analytis JG, De Greve K, McMahon PL, Islam Z, Yamamoto Y, et al. In-Plane Resistivity Anisotropy in an Underdoped Iron Arsenide Superconductor. *Science* (2010) 329:824–6. doi:10.1126/science.1190482
57. Ren X, Duan L, Hu Y, Li J, Zhang R, Luo H, et al. Nematic Crossover inBaFe2As2under Uniaxial Stress. *Phys Rev Lett* (2015) 115:197002. doi:10.1103/PhysRevLett.115.197002
58. Man H, Zhang R, Park JT, Lu X, Kulda J, Ivanov A, et al. Direct Observation of Spin Excitation Anisotropy in the Paramagnetic Orthorhombic State of BaFe2−xNixAs2. *Phys Rev B* (2018) 97:060507(R). doi:10.1103/PhysRevB.97.060507
59. Wiecki P, Zhou R, Julien MH, Böhmer AE, Schmalian J. Edwards-Anderson Parameter and Local Ising Nematicity in FeSe Revealed via NMR Spectral Broadening. *Phys Rev B* (2021) 104:125134. doi:10.1103/PhysRevB.104.125134
60. Lahiri A, Klein A, Fernandes RM. Defect-induced Electronic Smectic State at the Surface of Nematic Materials. *ArXiv* (2021) 2111:00541. doi:10.48550/arXiv.2111.00541
61. Li J, Zhao D, Wu YP, Li SJ, Song DW, Zheng LX, et al. Reemergeing Electronic Nematicity in Heavily Hole-Doped Fe-Based Superconductors. *ArXiv* (2021) 1611:04694. doi:10.48550/arXiv.1611.04694
62. Liu X, Tao R, Ren M, Chen W, Yao Q, Wolf T, et al. Evidence of Nematic Order and Nodal Superconducting gap along [110] Direction in RbFe2As2. *Nat Commun* (2019) 10:1039. doi:10.1038/s41467-019-08962-z
63. Moroni M, Prando G, Aswartham S, Morozov I, Bukowski Z, Büchner B, et al. Charge and Nematic Orders in AFe2As2(A=Rb,Cs) Superconductors. *Phys Rev B* (2019) 99:235147. doi:10.1103/physrevb.99.235147
64. Ishida K, Tsujii M, Hosoi S, Mizukami Y, Ishida S, Iyo A, et al. Novel Electronic Nematicity in Heavily Hole-Doped Iron Pnictide Superconductors. *Proc Natl Acad Sci U.S.A* (2020) 117:6424–9. doi:10.1073/pnas.1909172117
65. Wiecki P, Haghighirad AA, Weber F, Merz M, Heid R, Böhmer AE. Dominant In-Plane Symmetric Elastoresistance in CsFe2As2. *Phys Rev Lett* (2020) 125: 187001. doi:10.1103/PhysRevLett.125.187001
66. Wiecki P, Frachet M, Haghighirad AA, Wolf T, Meingast C, Heid R, et al. Emerging Symmetric Strain Response and Weakening Nematic Fluctuations in Strongly Hole-Doped Iron-Based Superconductors. *Nat Commun* (2021) 12:4824. doi:10.1038/s41467-021-25121-5
67. Borisov V, Fernandes RM, Valentí R. Evolution from B2g Nematics to B1g Nematics in Heavily Hole-Doped Iron-Based Superconductors. *Phys Rev Lett* (2019) 123:146402. doi:10.1103/PhysRevLett.123.146402
68. Wu YP, Zhao D, Wang AF, Wang NZ, Xiang ZJ, Luo XG, et al. Emergent Kondo Lattice Behavior in Iron-Based SuperconductorsAFe2As2(A=K, Rb, Cs). *Phys Rev Lett* (2016) 116:147001. doi:10.1103/PhysRevLett.116.147001
69. Civardi E, Moroni M, Babij M, Bukowski Z, Carretta P. Superconductivity Emerging from an Electronic Phase Separation in the Charge Ordered Phase of RbFe2As2. *Phys Rev Lett* (2016) 117:217001. doi:10.1103/PhysRevLett.117.217001

70. Baym G, Kadanoff LP. Conservation Laws and Correlation Functions. *Phys Rev* (1961) 124:287–99. doi:10.1103/physrev.124.287
71. Allen S, Tremblay AMS, Vilk YM. *Theoretical Methods for Strongly Correlated Electrons*. New-York: Springer-Verlag (2004).
72. Blaha P, Schwarz K, Tran F, Laskowski R, Madsen GKH, Marks LD. WIEN2k: An APW+lo Program for Calculating the Properties of Solids. *J Chem Phys* (2020) 152:074101. doi:10.1063/1.5143061
73. Mostofi AA, Yates JR, Pizzi G, Lee YS, Souza I, Vanderbilt D, et al. An Updated Version of Wannier90: A Tool for Obtaining Maximally-Localised Wannier Functions. *Comput Phys Commun* (2014) 185:2309–10. doi:10.1016/j.cpc.2014.05.003
74. Miyake T, Nakamura K, Arita R, Imada M. Comparison of Ab Initio Low-Energy Models for LaFePO, LaFeAsO, BaFe2As2, LiFeAs, FeSe, and FeTe: Electron Correlation and Covalency. *J Phys Soc Jpn* (2010) 79:044705. doi:10.1143/JPSJ.79.044705
75. Bickers NE, White SR. Conserving Approximations for Strongly Fluctuating Electron Systems. II. Numerical Results and Parquet Extension. *Phys Rev B* (1911) 43:8044–64. doi:10.1103/PhysRevB.43.8044
76. Kontani H, Yamakawa Y, Tazai R, Onari S. Odd-parity Spin-Loop-Current Order Mediated by Transverse Spin Fluctuations in Cuprates and Related Electron Systems. *Phys Rev Res* (2021) 3:013127. doi:10.1103/PhysRevResearch.3.013127
77. Nakayama K, Tsubono R, Phan GN, Nabeshima F, Shikama N, Ishikawa T, et al. Orbital Mixing at the Onset of High-Temperature Superconductivity in FeSe1−xTex/CaF2. *Phys Rev Res* (2021) 3:L012007. doi:10.1103/PhysRevResearch.3.L012007
78. Zhang P, Wang Z, Wu X, Yaji K, Ishida Y, Kohama Y, et al. Multiple Topological States in Iron-Based Superconductors. *Nat Phys* (2019) 15:41–7. doi:10.1038/s41567-018-0280-z
79. Wang Z, Zhang P, Xu G, Zeng LK, Miao H, Xu X, et al. Topological Nature of theFeSe0.5Te0.5superconductor. *Phys Rev B* (2015) 92:115119. doi:10.1103/PhysRevB.92.115119
80. Lohani H, Hazra T, Ribak A, Nitzav Y, Fu H, Yan B, et al. Band Inversion and Topology of the Bulk Electronic Structure in FeSe0.45Te0.55. *Phys Rev B* (2020) 101:245146. doi:10.1103/PhysRevB.101.245146
81. Yin ZP, Haule K, Kotliar G. Kinetic Frustration and the Nature of the Magnetic and Paramagnetic States in Iron Pnictides and Iron Chalcogenides. *Nat Mater* (2011) 10:932–5. doi:10.1038/nmat3120
82. Yamasaki A, Matsui Y, Imada S, Takase K, Azuma H, Muro T, et al. Electron Correlation in the FeSe Superconductor Studied by Bulk-Sensitive Photoemission Spectroscopy. *Phys Rev B* (2010) 82:184511. doi:10.1103/PhysRevB.82.184511
83. Watson MD, Haghighirad AA, Rhodes LC, Hoesch M, Kim TK. Electronic Anisotropies Revealed by Detwinned Angle-Resolved Photo-Emission Spectroscopy Measurements of Fese. *New J Phys* (2017) 19:103021. doi:10.1088/1367-2630/aa8a04
84. Yi M, Pfau H, Zhang Y, He Y, Wu H, Chen T, et al. Nematic Energy Scale and the Missing Electron Pocket in FeSe. *Phys Rev X* (2019) 9:041049. doi:10.1103/PhysRevX.9.041049
85. Huh SS, Seo JJ, Kim BS, Cho SH, Jung JK, Kim S, et al. Absence of Y-Pocket in 1-Fe Brillouin Zone and Reversed Orbital Occupation Imbalance in FeSe. *Commun Phys* (2020) 3:52. doi:10.1038/s42005-020-0319-1
86. Rhodes LC, Boker J, Muller MA, Eschrig M, Eremin IM. Non-local D_{xy} Nematicity and the Missing Electron Pocket in FeSe. *npj Quan Mater* (2021) 6:45. doi:10.1038/s41535-021-00341-6
87. Tazai R, Matsubara S, Yamakawa Y, Onari S, Kontani H. A Rigorous Formalism of Unconventional Symmetry Breaking in Fermi Liquid Theory and its Application to Nematicity in FeSe. *ArXiv* (2022) 2205:02280. doi:10.48550/arXiv.2205.02280
88. Moon SJ, Schafgans AA, Kasahara S, Shibauchi T, Terashima T, Matsuda Y, et al. Infrared Measurement of the Pseudogap of P-Doped and Co-doped High-TemperatureBaFe2As2Superconductors. *Phys Rev Lett* (2012) 109:027006. doi:10.1103/PhysRevLett.109.027006
89. Shimojima T, Sonobe T, Malaeb W, Shinada K, Chainani A, Shin S, et al. Pseudogap Formation above the Superconducting Dome in Iron Pnictides. *Phys Rev B* (2014) 89:045101. doi:10.1103/PhysRevB.89.045101
90. Shimojima T, Malaeb W, Nakamura A, Kondo T, Kihou K, Lee CH, et al. Antiferroic Electronic Structure in the Nonmagnetic Superconducting State of the Iron-Based Superconductors. *Sci Adv* (2017) 3:e1700466. doi:10.1126/sciadv.1700466
91. Yi M, Lu D, Chu JH, Analytis JG, Sorini AP, Kemper AF, et al. Symmetry-breaking Orbital Anisotropy Observed for Detwinned Ba(Fe 1- X Co X) 2 as 2 above the Spin Density Wave Transition. *Proc Natl Acad Sci U.S.A* (2011) 108:6878–83. doi:10.1073/pnas.1015572108
92. Zhou R, Xing LY, Wang XC, Jin CQ, Zheng GQ. Orbital Order and Spin Nematicity in the Tetragonal Phase of the Electron-Doped Iron pnictidesNaFe1−xCoxAs. *Phys Rev B* (2016) 93:060502(R). doi:10.1103/PhysRevB.93.060502
93. Mizukami Y, Tanaka O, Ishida K, Tsujii M, Mitsui T, Kitao S, et al. Thermodynamic Signatures of Diagonal Nematicity in $RbFe_2As_2$ Superconductor. *ArXiv* (2021) 2108:13081. doi:10.48550/arXiv.2108.13081
94. Tsuchiizu M, Ohno Y, Onari S, Kontani H. Orbital Nematic Instability in the Two-Orbital Hubbard Model: Renormalization-Group + Constrained RPA Analysis. *Phys Rev Lett* (2013) 111:057003. doi:10.1103/PhysRevLett.111.057003
95. Yamakawa Y, Onari S, Kontani H (2022). Unpublished.

Conflict of Interest: The authors declare that the research was conducted in the absence of any commercial or financial relationships that could be construed as a potential conflict of interest.

Publisher's Note: All claims expressed in this article are solely those of the authors and do not necessarily represent those of their affiliated organizations, or those of the publisher, the editors, and the reviewers. Any product that may be evaluated in this article, or claim that may be made by its manufacturer, is not guaranteed or endorsed by the publisher.